

The structure of the superconducting high-pressure phase of Sc_3CoC_4

Jan Langmann,¹ Marcel Vöst,¹ Dominik Schmitz,¹ Christof Haas,¹

Georg Eickerling,^{1,*} Anton Jesche,² Michael Nicklas,³ Arianna

Lanza,⁴ Nicola Casati,⁵ Piero Macchi,⁶ and Wolfgang Scherer^{1,†}

¹*CPM, Institut für Physik, Universität Augsburg, D-86159 Augsburg, Germany*

²*Experimentalphysik VI, Zentrum für Elektronische Korrelation und Magnetismus,
Institut für Physik, Universität Augsburg, D-86159 Augsburg, Germany*

³*Max Planck Institute for Chemical Physics of Solids,
Nöthnitzer Straße 40, D-01087 Dresden, Germany*

⁴*Center for Nanotechnology Innovation@NEST,
Istituto Italiano di Tecnologia, I-56127 Pisa, Italy*

⁵*Swiss Light Source, Paul Scherrer Institut, CH-5232 Villigen, Switzerland*

⁶*Dipartimento di Chimica, Materiali ed Ingegneria Chimica “G. Natta”,
Politecnico di Milano, I-20133 Milano, Italy*

(Dated: December 31, 2021)

Abstract

We investigate pressure-induced structural changes to the Peierls-type distorted low-temperature phase of the low-dimensional Sc_3CoC_4 as a possible origin of its pressure-enhanced superconductivity. By means of cryogenic high-pressure x-ray diffraction experiments we could reveal subtle, but significant structural differences between the low-temperature phase at ambient and elevated pressures. We could thus establish the structure of the superconducting phase of the title compound which interestingly still shows the main features of the Peierls-type distorted low-temperature phase. This indicates that in contrast to other low-dimensional materials a suppression of periodic structural distortions is no prerequisite for superconductivity in the transition metal carbide.

I. INTRODUCTION

Structurally low-dimensional materials and dimensionality-driven physical effects are making their way into technical applications. Quantum dots (0D) are actively deployed in display technology^{1,2} or under intensive research for future uses in quantum computing.³ Nano-wires (1D) enable great improvements in photo- and chemo-electric detectors and thermoelectric devices.⁴ Transistors fabricated of atomically thin graphene layers (2D) might become an integral part of post-silicon microprocessors.^{5,6} Furthermore, 3D superstructures of thin metal layers – arranged in the right way to break inversion symmetry – might provide promising candidates for diodes in superconducting electronics.⁷

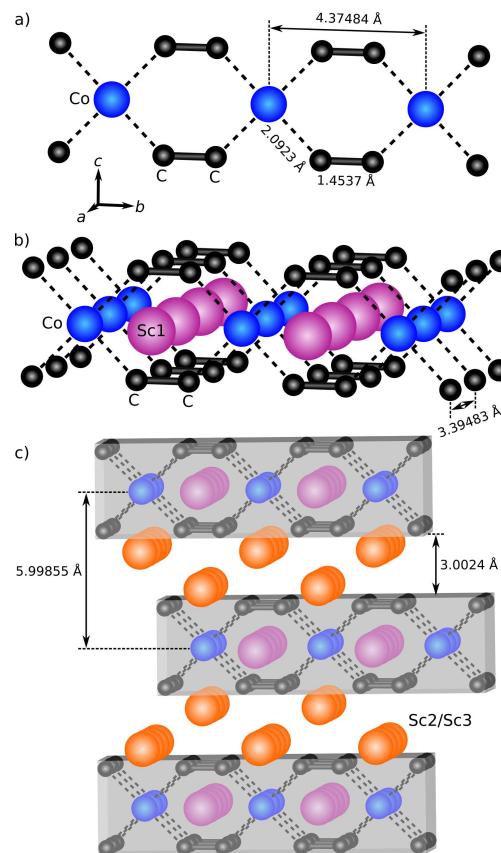


FIG. 1. (a) Infinite $[\text{Co}(\text{C}_2)_2]_\infty$ ribbon as basic quasi-1D building unit of the Sc_3CoC_4 structure; (b) composition of a quasi-2D layer by stacking $[\text{Co}(\text{C}_2)_2]_\infty$ ribbons and Sc1 atoms along the a axis of the orthorhombic high-temperature phase; (c) decoupling of the quasi-2D layers along the c axis by interleaved Sc2 and Sc3 atoms. Salient inter-atomic distances are specified (structural data from Ref. 8).

As indicated by the last example, the combination of structural low dimensionality with superconductivity can stimulate intriguing effects, even though W. A. Little’s prediction of room-temperature superconductivity in quasi-one-dimensional materials^{9,10} still remains an unobserved phenomenon at ambient pressure. Instead, a rich playing field of different ordering phenomena interacting with superconductivity has unfolded, *e.g.* structural transitions, charge- and spin-density waves, and antiferromagnetism.^{11–21} Superconducting compounds with intrinsically low-dimensional character have a special appeal to solid-state sciences, although the synthesis of large and defect-free single crystals is often challenging. This, for example, becomes evident from the large number of publications devoted to the well-known quasi-one-dimensional NbSe₃^{14,15,22,23} or quasi-two-dimensional graphite/graphene^{24,25} and transition-metal dichalcogenides.^{11,26–30}

The transition-metal carbide Sc₃CoC₄ crystallizes in a structure type combining quasi-1D and quasi-2D features. Quasi-1D [Co(C₂)₂]_∞ ribbons extending along the crystallographic *b* axis of the orthorhombic unit cell (Fig. 1a) are formed by covalent bonds between the cobalt atoms and C₂ moieties.³¹ Alternating stacking of the [Co(C₂)₂]_∞ ribbons and scandium atoms (Sc1) along the *a* axis leads to quasi-2D layers (Fig. 1b). Therein, neighboring [Co(C₂)₂]_∞ ribbons with a separation of 3.39483(3) Å are held together by subtle Sc-C₂ interactions. Additional scandium atom layers (Sc2 and Sc3; Fig. 1c) are interleaved along the *c* axis resulting in a large interlayer distance of 5.99855(5) Å between adjacent Sc1-Co-C layers.^{8,31–37}

Superconductivity in Sc₃CoC₄ emerges below $T_c \approx 4.5$ K^{8,34,35} and is anticipated by a Peierls-type structural transition below 72 K.⁸ Therein, the orthorhombic high-temperature (HT) phase structure (space group *Immm*) is transformed into the monoclinic low-temperature (LT) phase structure (space group *C2/m*) by a doubling of the translational period along the [Co(C₂)₂]_∞ ribbons.^{8,34,36,38} The exact degree and mode of interaction between this structural HT→LT phase transition and the onset of superconductivity at even lower temperatures is, however, not fully established yet. Furthermore, high-pressure studies of the electrical resistivity and magnetization in polycrystalline samples by Wang *et al.*³⁹ revealed a drastic increase of the superconducting volume at virtually constant T_c values. The authors rationalized this behavior by a pressure- and temperature-controlled coexistence of the HT and LT phase in the compound, whereby only the HT phase was supposed to become superconducting.³⁹ But no structural information to verify this hypothesis has been pro-

vided up to now. Therefore, we performed high-pressure and low-temperature single-crystal x-ray diffraction studies in combination with physical property measurements to explore the pressure- and temperature-dependent structure-property relationship in Sc_3CoC_4 .

II. METHODS

Single- and polycrystalline samples of Sc_3CoC_4 were synthesized by arc-melting according to the method described in the literature^{31,37,40} and in addition from a lithium metal flux.^{41,42} Needle-like samples were obtained from arc-melting and platelet-like samples from crystallization in a lithium flux (full details of the synthesis and characterization methods employed can be found in the Supplemental Material⁴³).

Magnetization measurements on a single-crystalline Sc_3CoC_4 sample were performed at various pressures up to 1.48 GPa using a miniature Ceramic Anvil Cell (mCAC)^{44–48} assembled with a Cu:Be gasket. The respective pressures were determined at low temperatures by reference to the pressure dependence of T_c for an additional lead piece inside the pressure chamber.^{49,50} Both, single-crystal and lead pressure gauge, were surrounded by Daphne 7373^{51,52} serving as a pressure transmitting medium. Supplemental ambient-pressure measurements before and after the high-pressure study were performed by gluing the sample to a glass rod with GE Varnish. For all magnetization measurements a QUANTUM DESIGN MPMS3 SQUID magnetometer was employed. The superconducting properties of the Sc_3CoC_4 sample were investigated by cooling the pressure cell or glass rod to 1.8 K under zero-field-cooling conditions and recording the temperature-dependent magnetization while heating from 1.8 K to 9 K in a magnetic field of 5 Oe.

High-pressure electrical resistivity measurements up to 1.26 GPa were performed employing a piston-cylinder-type pressure cell and silicon oil as pressure-transmitting medium. The single-crystalline Sc_3CoC_4 whisker was contacted by a four-point configuration using silver conductive paint and gold filaments. The pressure inside the pressure chamber was determined at low temperatures by measuring the shift of the superconducting transition temperature of a piece of lead.^{49,50} For details of the setup see Ref. 53. The temperature-dependent resistivity measurements were carried out for various applied pressures upon cooling and heating cycles between 1.8 K and 300 K in a QUANTUM DESIGN PPMS using a LINEAR RESEARCH LR700 resistance bridge.⁵⁴ Additional ambient-pressure mea-

measurements of single-crystalline Sc_3CoC_4 whiskers four-point contacted with silver-epoxy resin were taken without surrounding pressure cell and using the standard DC-resistivity option of a QUANTUM DESIGN PPMS. Uniaxial strain was created by gluing both ends of a whisker to a sapphire substrate using large droplets of silver-epoxy resin.

Pressure-dependent lattice parameters at room temperature were obtained from Le Bail fits^{55,56} of synchrotron powder x-ray diffraction data with the software JANA2006.⁵⁷ The respective diffraction experiments were carried out at the X04SA Materials Science (MS) beamline at the Swiss Light Source (SLS)^{58,59} using a PSI Mythen II one-dimensional detector⁶⁰ and a membrane-driven diamond anvil cell (DAC). The pressure chamber was filled with finely ground and sieved Sc_3CoC_4 powder (nominal sieve opening $32\ \mu\text{m}$), and a 4:1 volume mixture of methanol and ethanol⁶¹ was used as pressure-transmitting medium. α -quartz powder was added for pressure calibration by reference to its well-known equation of state.⁶²

The single-crystal x-ray diffraction data in this work was collected on a HUBER four-circle Eulerian cradle goniometer equipped with a DECTRIS Pilatus CdTe 300K pixel detector and an INCOATEC AgK_α microfocus sealed-tube x-ray source ($\lambda = 0.56087\ \text{\AA}$).

High-pressure low-temperature x-ray diffraction studies of Sc_3CoC_4 single crystals up to a pressure of 5.5 GPa were carried out using a Diacell Tozer-type DAC^{63,64} and Daphne 7575 as pressure-transmitting medium.⁶⁵ Ruby spheres inside the pressure chamber allowed a pressure determination at room temperature *via* the ruby fluorescence method.⁶⁶⁻⁶⁸ Sample cooling to temperatures above 20 K was achieved utilizing an ARS closed-cycle helium cryocooler with exchangeable vacuum and radiation shields surrounding the Tozer-type DAC. The temperature-dependence of selected reflection intensities at various applied pressures was tracked with a stainless steel vacuum chamber featuring kapton windows. To collect x-ray diffraction data for structure determinations at pressures of 0 GPa and 4 GPa and temperatures of approx. 40 K and 110 K the stainless steel vacuum chamber was replaced by a beryllium vacuum dome providing a larger accessible reciprocal space fraction.

A similar experimental setup featuring the closed-cycle helium cryocooler and an outer and inner beryllium vacuum and radiation shield was used to obtain single-crystal x-ray diffraction data at ambient pressure and sample temperatures of 11 K, 70 K and 100 K.

For high-pressure x-ray diffraction measurements on a Sc_3CoC_4 single-crystal up to 10.1 GPa at room temperature a Boehler-plate-type DAC^{64,69} was employed. The filling procedure and pressure determination method were analogous to the experiments with the

Tozer-type DAC described above, but with a 4:1 volume mixture of methanol and ethanol⁶¹ as pressure-transmitting medium.

Obtained x-ray diffraction intensities were evaluated using the EVAL14 suite of programs^{70,71} and subjected to scaling and absorption correction using the programs SADABS/TWINABS.⁷² More information on the handling of parasitic scattering and shadowing of the x-ray beam by high-pressure or low-temperature equipment is available in the Supplemental Material.⁴³ Structural refinements were performed with the program JANA2006.⁵⁷

Density Functional Theory (DFT) calculations on the HT phase of Sc_3CoC_4 were performed employing the VASP code.^{73–76} The PBE density functional,^{77,78} an energy cutoff for the plane wave basis set of 500 eV and a Brillouin grid sampling of $4\times 4\times 2$ were used throughout. The starting geometry for the ambient pressure HT structure was adopted from the optimizations performed in Ref. 38, which are based on the same set of parameters.

Pressure-dependent geometry relaxations were performed at pressures of 2, 4, 6, 8 and 10 GPa. Optimizations were stopped when forces were smaller than 0.001 eV/Å. Single-point SCF calculations enforcing uniaxial strain were performed by reducing the a , b and c lattice parameters of the relaxed HT ambient pressure structure by ± 0.02 Å and ± 0.04 Å.

All phonon dispersion calculations employing the finite displacement approach in a $2\times 2\times 2$ supercell were performed with the PHONOPY code⁷⁹ and VASP as force calculator using the same parameters as specified above.

III. RESULTS AND DISCUSSION

Starting point of our study are the results published earlier by Wang *et al.*³⁹ These authors found a significant increase in the superconducting volume fraction of polycrystalline Sc_3CoC_4 samples under the application of modest hydrostatic pressures. In the present study, we performed physical property measurements and x-ray diffraction experiments on single-crystalline samples. This allows us to explore potential structure-property relationships in Sc_3CoC_4 and gain deeper insight into the origins of pressure-enhanced superconductivity in the low-dimensional material. Also for single-crystalline samples a clear superconducting signature is only observed in the electrical resistivity $\rho(T)$ (see Fig. 2a) and the magnetization $M(T)$ (Fig. 2b and Fig. 2c) after application of pressure. It is noteworthy that the enhanced superconducting signal persists for several hours after decreasing the

pressure from 1.48 GPa to 0.19 GPa. It remains remanently present even after removing the sample from the pressure cell (see Fig. 2c). This hints to a potential hysteretical behavior of the inherent structural changes induced by the application of pressure. Degradation of the sample quality as a possible origin of this behavior could be excluded by means of x-ray diffraction before and after performing a high-pressure experiment at 4.5 GPa and 27 K (see Supplemental Material⁴³).

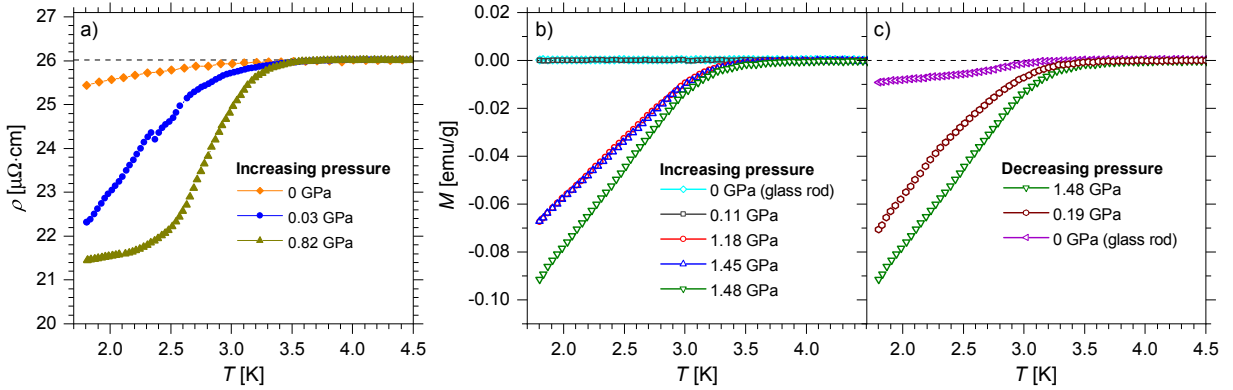


FIG. 2. Temperature- and pressure-dependent development of (a) the electrical resistivity $\rho(T)$ and (b, c) the magnetization $M(T)$ after zero-field-cooling in a magnetic field of 5 Oe for the superconducting transition of Sc_3CoC_4 . Data points in (a) and (b) were recorded while increasing the pressure and data points in (c) while decreasing the pressure. Note that the ambient-pressure measurements of $\rho(T)$ (a) and $M(T)$ (b, c) were performed without a pressure cell. For better comparability, data points were brought to overlap at 4.5 K by applying shifts along the ρ -/ M -axis.

In other low-dimensional compounds like the transition-metal dichalcogenides $1T$ -TiSe₂, $2H$ -TaSe₂ and $2H$ -NbSe₂ the pressure-induced emergence of superconductivity is intimately linked to the suppression of a periodic structural distortion at low temperatures, *i.e.* a commensurate or incommensurate charge-density wave.^{80–88} We therefore tried to clarify, whether the Peierls-type distortion leading to the low-temperature (LT) phase^{8,38} might be suppressed upon application of pressure to enhance the superconductivity in Sc_3CoC_4 .³⁹ The structural properties of the ambient-pressure low-temperature phase have been studied earlier⁸ and provide the starting point of this pressure- and temperature-dependent study. Atom displacements and bond lengths mentioned hereafter were determined in an ambient-pressure x-ray diffraction experiment on a high-quality single-crystalline needle of Sc_3CoC_4 at 11 K (see experimental section and Supporting Material⁴³ for further details). All bond

lengths and displacements in this work are given with their threefold standard deviation, while crystallographic directions are always specified with respect to the axes of the orthorhombic HT phase (space group $Immm$).

The LT phase of Sc_3CoC_4 (space group $C2/m$) is characterized by modulated displacements of Co, Sc1 and C atoms from their HT phase positions in the quasi-2D layers of the Sc_3CoC_4 structure (see Fig. 3a). Precisely, the cobalt atoms along a $[\text{Co}(\text{C}_2)_2]_\infty$ ribbon experience shifts of $\pm 0.11038(18)$ Å relative to their crystallographic $2d$ site in the HT phase (information on the calculation of the atom displacements is provided in the Supplemental Material⁴³). Hence, Co–Co distances within chains of cobalt atoms along the a axis display alternating larger ($3.5985(9)$ Å) and smaller ($3.1569(6)$ Å) values compared to the constant separation of $3.3948(12)$ Å in the HT phase.⁸ This modulation of the Co atomic positions is complemented by a modulation of the Sc1 atomic positions. Their displacements of $\pm 0.0574(3)$ Å with regard to the $2b$ HT positions point along the b axis and alternate along the a axis, *i.e.* their displacement direction is perpendicular to the modulation of the Co atomic positions. As can be seen in Fig. 3a, the modulation of the Co and Sc1 atoms is correlated in such a way that the Sc1 atoms are shifted towards long Co–Co contacts and evade short Co–Co contacts. In analogy to the arrangement of the cobalt atoms, this displacement pattern turns chains of equispaced scandium atoms along the b axis ($4.3748(12)$ Å) above and below the $[\text{Co}(\text{C}_2)_2]_\infty$ ribbons into chains with alternating longer ($4.5015(12)$ Å) and shorter ($4.2718(12)$ Å) Sc1–Sc1 distances.

As a consequence of the HT→LT transition the $[\text{Co}(\text{C}_2)_2]_\infty$ ribbons are no longer planar, which is also reflected by rotations of the C_2 units about rotation axes parallel to c . Due to the lack of a crystallographic m plane perpendicular to a rotations of adjacent C_2 units about the b axis in the same direction (conrotatory) or opposite directions (disrotatory) are both allowed by symmetry. The potential importance of the carbon atoms for superconductivity in Sc_3CoC_4 can be derived from isotopic substitution experiments: replacement of ^{12}C by ^{13}C leads to a systematic suppression of the superconducting onset temperature T_c^{onset} with an isotope coefficient α of 0.58.⁸⁹ This observation is in line with the predictions of a Density Functional Theory (DFT) study by Zhang *et al.*⁹⁰ The authors proposed that rotations of the C_2 units and cobalt and scandium atom displacements are integral parts of key phonon modes coupling conduction electrons into superconducting Cooper pairs.

Yet, rotations of the C_2 units are experimentally more difficult to assess by x-ray diffrac-

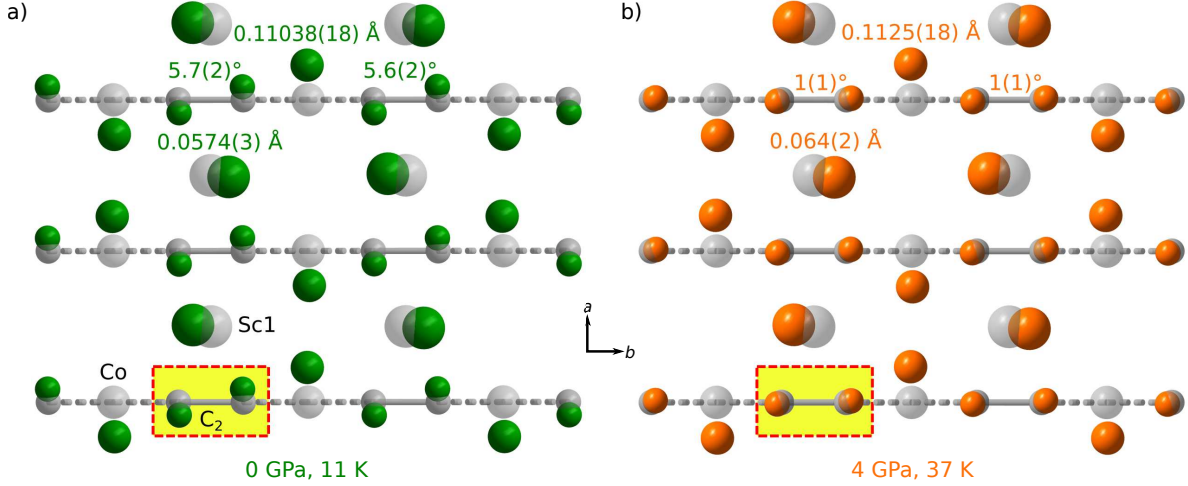


FIG. 3. Overlays of the refined atomic positions within a layered building unit of Sc_3CoC_4 at room temperature (gray, semi-transparent; atomic positions from Ref. 8) and after cooling to low temperatures (a) without or (b) with applied pressure (colored, non-transparent). All atom displacements are exaggerated seven-fold, Sc2 and Sc3 atoms have been omitted for clarity. Specified values of atom displacements and rotation angles are given with their threefold standard deviation.

tion than shifts of the heavy atoms cobalt and scandium. The latter displacements invariably lead to the appearance of prominent superstructure reflections with $k = (+\frac{1}{2}, +\frac{1}{2}, 0)$ and also with $k' = (+\frac{1}{2}, -\frac{1}{2}, 0)$ due to systematic pseudo-merohedric twinning⁹¹ (see Fig. 6f).^{8,38,40} By contrast, carbon atom displacements may only contribute to the superstructure reflections in the case of disrotatory displacements of neighboring C_2 units (a more detailed discussion can be found in the Supplemental Material⁴³). Conrotatory displacements make no contribution to the intensities of the superstructure reflections, and only a minor contribution to the intensities of the main reflections, *i.e.* even a hypothetical rotation by 15° changes the average main reflection intensity by less than 1 %. To obtain precise intensity information for main and superstructure reflections we therefore employed long exposure times, a high-brilliance microfocus x-ray source and a noise-reduced pixel detector with high dynamic range for the single-crystal x-ray diffraction experiments discussed in the following (see the experimental section and the Supporting Material⁴³ for more details).

Our structural model at 11 K and ambient pressure is characterized by rotations of the two symmetry-independent C_2 units in the same direction with rotation angles of $5.6(2)^\circ$ and $5.7(2)^\circ$ (highlighted in Fig. 3a). Similar carbon atom shifts resulting in somewhat

smaller but still conrotatory rotation angles of $2.8(4)^\circ$ and $3.0(4)^\circ$ have been found earlier at 9 K.⁸ Notably, the observed conrotatory displacements of subsequent C_2 units along the $[Co(C_2)_2]_\infty$ ribbons result in the formation of shorter ($2.098(4)$ Å) and longer ($2.113(3)$ Å) Co-C distances in contrast to an alternative scenario with disrotatory displacements which would minimize all Co-C distances. This rules out that strengthening of Co-C bonds provides the only driving force of the carbon atom shifts in the LT phase structure.

In the next steps of our analysis we will aim at establishing possible pressure-dependent structure-property relationships to gain further insight into the potential origins of the characteristic superconducting behavior of Sc_3CoC_4 . Measurements of the electrical resistivity $\rho(T)$ already hint towards potential pressure-induced modifications of our reference LT phase structure: As outlined earlier,³⁸ the extended phonon softening process leading to a static Peierls-type structural distortion of Sc_3CoC_4 at ambient pressure is delimited by two pronounced anomalies in $\rho(T)$ at 152 K and 83 K (Fig. 4a). Our high-pressure experiments on single-crystalline samples in accordance with Wang *et al.*³⁹ show that only a single broad anomaly at 156 K can be observed in $\rho(T)$ after application of 0.03 GPa (see blue curve in Fig. 4b). This anomaly further shifts towards higher temperatures with increasing pressure (dark yellow curve in Fig. 4b). A similar result, *i.e.* a suppression of the first anomaly at lower temperature in $\rho(T)$ and an upward shift of the second one by approx. 10 K, can be obtained by fixing a single-crystalline Sc_3CoC_4 needle at two points along its long axis (*i.e.* parallel to the crystallographic a axis) on top of a sapphire chip (see Fig. 4c).

In order to investigate the origin of these pressure-dependent changes in $\rho(T)$ we performed x-ray diffraction experiments at variable pressure and temperature. Inspection of Bragg intensities as well as atomic positions from structural refinements should reveal, whether (*i*) only the distortion pattern during the HT→LT phase transition changes under pressure, (*ii*) the structurally distorted LT phase is suppressed in favor of the undistorted HT phase,³⁹ or (*iii*) a designated and structurally distinct high-pressure LT phase of Sc_3CoC_4 is formed.

In support of hypothesis (*i*), our measurements indicate that the low-temperature superstructure Bragg reflections with $k = (+\frac{1}{2}, +\frac{1}{2}, 0)$ can be observed up to pressures of 5.5 GPa. No indication for a pressure-induced structural phase transition connected with a change of the space group can be found. Instead, the collected diffraction data can still be described by a monoclinic lattice and complies with space group $C2/m$. Differences between pressurized

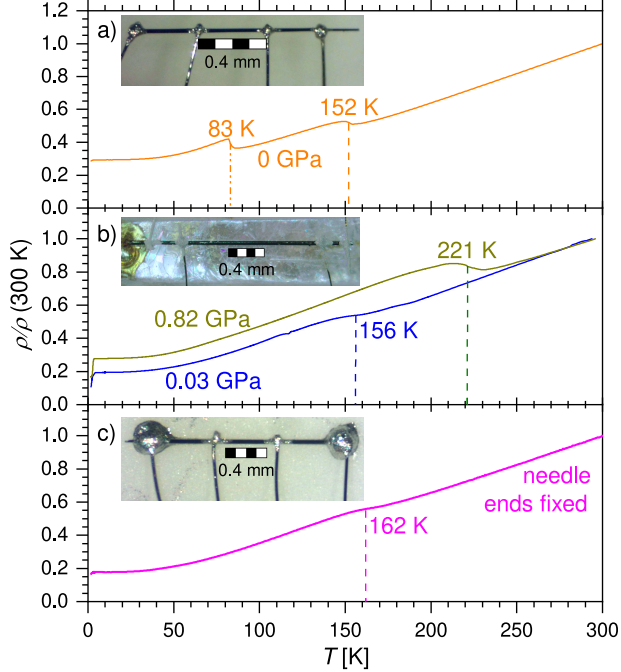


FIG. 4. Temperature-dependent electrical resistivity $\rho(T)$ of Sc_3CoC_4 single-crystals (a) at ambient pressure and without fixation to a substrate, (b) at hydrostatic pressures of 0.03 GPa and 0.82 GPa and (c) glued at both ends on top of a sapphire chip. Insets: Photographic images of the respective samples after their preparation for measurements (a) to (c).

and unpressurized samples, however, may be recognized by comparing reconstructions of the $(h, 0.5, l)$ reciprocal space plane at 22 K for pressures between 0 GPa and 5.5 GPa (Fig. 5). Note that at ambient pressure Sc_3CoC_4 crystals in the LT phase are systematically twinned with each of the two differently oriented twin domains contributing half of the superstructure reflections to the $(h, 0.5, l)$ plane (green and orange circles in Fig. 5). Cooling crystals below the HT \rightarrow LT phase transition temperature at elevated pressures reveals that one half of the superstructure reflections shows increasing intensities, whereas the other half shows decreasing intensities ($p \leq 1.9$ GPa). The latter superstructure reflections finally vanish completely for $p > 1.9$ GPa, thus indicating a pressure-induced detwinning of the crystal.⁹²

Taking into account the otherwise unchanged characteristics of the LT phase in reciprocal space we may connect the strongly modified behavior of the anomalies in $\rho(T)$ under pressure (compare Fig. 4a and Fig. 4b) to changes along the pathway from the HT to the LT phase. Therefore, we determined the temperature- and pressure-dependence of the scattered intensity $I_{\text{XRD}}(T, p)$ at the positions of representative superstructure reflections (see Fig. 6).

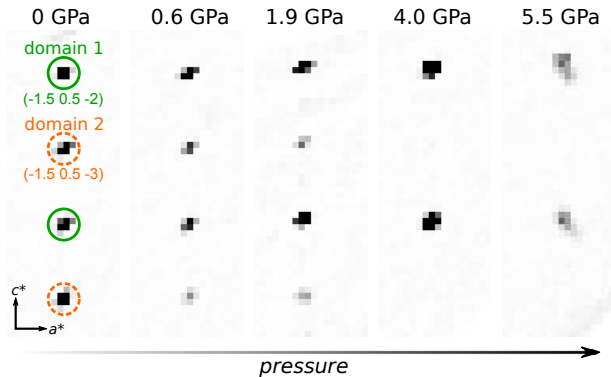


FIG. 5. Pressure-induced detwinning of a Sc_3CoC_4 sample at $T = 22$ K, as observed by x-ray diffraction in case of characteristic Bragg reflections from two twin domains (twin law $[[-1 \ 0 \ 0], [0 \ 1 \ 0], [0 \ 0 \ 1]]$, *i.e.* an m plane perpendicular to the a axis of the orthorhombic HT unit cell). The displayed sections of the $(h, 0.5, l)$ plane contain only superstructure reflections and were recorded after applying pressures up to 5.5 GPa and cooling to 22 K. The decreased scattering intensity at 5.5 GPa is due to a beginning deterioration of the sample crystallinity.

Consistent with $\rho(T)$, the increase of $I_{\text{XRD}}(T, p)$ with decreasing temperature, which occurs in two steps at ambient pressure (Fig. 6a), renders into a continuous increase under pressure (Fig. 6b to Fig. 6e). We note, however, that a quantitative comparison of applied pressure values in $\rho(T)$ and $M(T)$ studies with those of the x-ray diffraction experiments is hampered by the differing sample environments and pressure determination methods employed (see experimental section and Supplemental Material⁴³).

From our data we may conclude that the LT phase is stabilized substantially, as is indicated by a shift of the onset temperature of the superstructure reflection intensities from 142 K at 0 GPa (Fig. 6a) to 231 K at 4 GPa (Fig. 6d). A pressure of 5.5 GPa preserves the superstructure reflections up to room temperature (Fig. 6e, see also the Supplemental Material⁴³), although at the cost of a degradation of the sample crystallinity. Interestingly, the isoelectronic and isostructural transition metal carbides Sc_3IrC_4 and Sc_3RhC_4 also show a periodically distorted structure in analogy to the LT phase of Sc_3CoC_4 at room temperature but without prior cooling or pressure application.^{93,94} There are, however, neither hints to superconductivity nor to the existence of an undistorted high-temperature phase comparable to Sc_3CoC_4 for these highly related compounds. In particular, systematic twinning as indicator of a potential t_2 HT \rightarrow LT transition has not been observed in the iridium

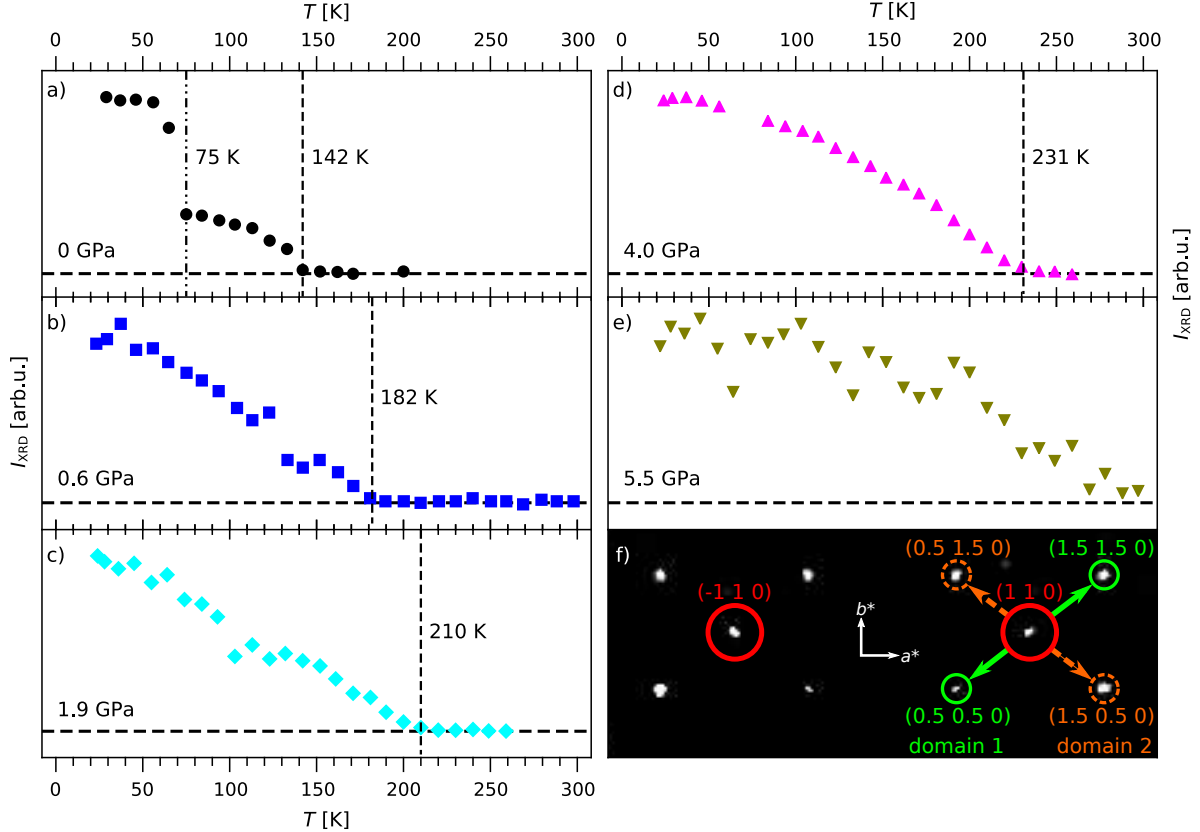


FIG. 6. Temperature-dependence of the scattered intensity $I_{\text{XRD}}(T, p)$ at the positions of representative superstructure reflections for pressures between 0 GPa (a) and 5.5 GPa (e). A section of the $(hk0)$ plane (f) illustrates the location of the superstructure reflections for twin domains 1 and 2 with respect to the main reflections.

and rhodium congeners of Sc_3CoC_4 .⁹⁴ This discrepancy may be due to the fact that the $3d$ metal cobalt is characterized by a significantly smaller covalent radius and weaker transition metal-carbon bonds in comparison with the $4d$ and $5d$ group members rhodium and iridium. The resulting higher structural flexibility of Sc_3CoC_4 could thus be a prerequisite to allow the existence of both, a HT and a LT phase structure.

The occurrence of a subtle competition between the HT and LT phase in Sc_3CoC_4 is reflected in the extended phonon softening regime preceding the HT \rightarrow LT transition at ambient-pressure.³⁸ Also its signatures in the temperature dependencies of $\rho(T)$ (Fig. 4a) and $I_{\text{XRD}}(T, p)$ (Fig. 6a) react sensitively and in a highly related way already to small changes in pressure. Application of a pressure below 0.6 GPa is sufficient to induce a cross-over of both physical properties from a course with two anomalies limiting the phonon softening

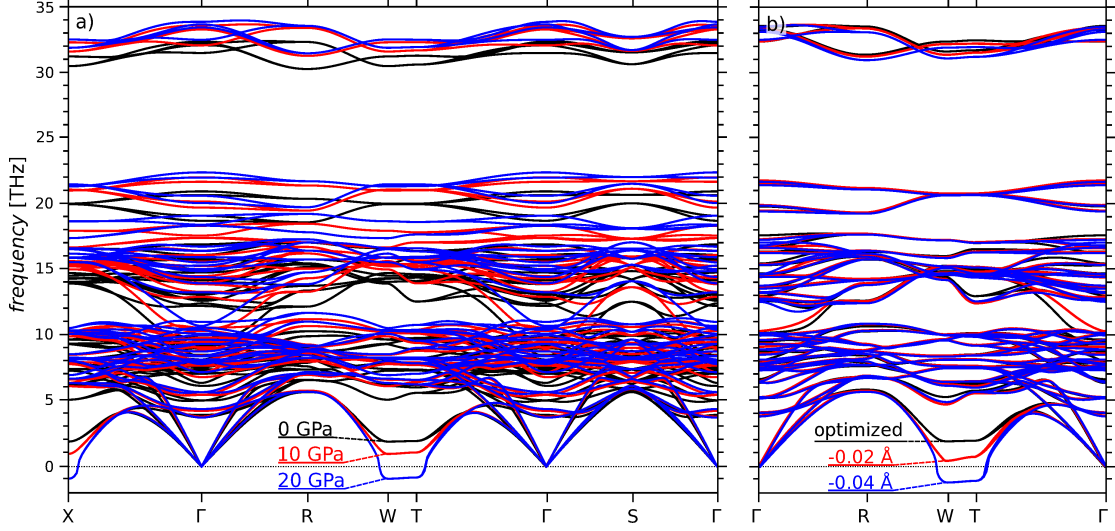


FIG. 7. Response of the phonon dispersion of HT Sc_3CoC_4 (DFT study) to (a) hydrostatic pressure, and (b) to a reduction of the lattice parameter a .

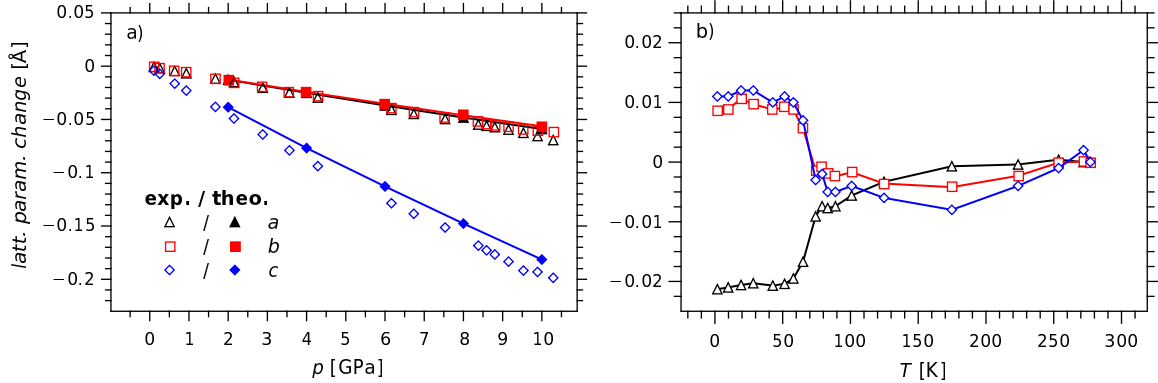


FIG. 8. Changes of the experimental (empty symbols) and theoretical (filled symbols) lattice parameters of Sc_3CoC_4 (a) with varying pressure at constant temperature and (b) with varying temperature at ambient pressure (data from Ref. 8).

regime towards low and high temperatures³⁸ to a course with a single anomaly (see Fig. 4b and Fig. 6b to Fig. 6e). Unfortunately, x-ray scattering and absorption by the employed pressure cell did not permit the investigation of the very weak and diffuse x-ray scattering features in analogy to Ref. 38. Pressure-dependent *ab initio* phonon dispersion calculations for the HT phase structure, however, can provide more insight into the underlying causes for the modification of $\rho(T)$ and $I_{\text{XRD}}(T, p)$ under pressure. Fig. 7a illustrates the presence of a soft branch between the high-symmetry points W and T of the phonon dispersion

already at ambient-pressure conditions. The phonon mode along the branch is characterized by displacements of the cobalt and scandium atoms (Sc1) in the ab plane anticipating their displacements in the LT phase of Sc_3CoC_4 (see Fig. 3a).³⁸ On progressing along the path from T to W the LT-phase-like pattern of atomic displacements at T is modified by modulations of decreasing wave length along the c axis. Yet, carbon atom contributions to the mode in analogy to the displacements shown in Fig. 3a are absent. These can be found in a separate medium-frequency phonon mode at Γ with still unclear behavior upon cooling below the HT \rightarrow LT phase transition temperature. So far, there is only evidence for a profound temperature-dependence of the W–T phonon branch. Approaching the HT \rightarrow LT transition temperature from above results in a reduction of the phonon frequency at T to zero.³⁸ The same W–T phonon branch also displays an extraordinary sensitivity to hydrostatic pressure (see Fig. 7a and the Supplemental Material⁴³). Its frequency is subjected to a strong and steady red shift with increasing pressure, while the frequencies of all other phonon branches show the expected blue shift. These trends indicate a gradual destabilization of the HT phase structure with increasing pressure in line with the experimentally observed pressure-induced enhancement of the transition temperature from the HT to the LT phase.⁹⁵

Despite the red frequency shift of the W–T phonon branch in our calculations (Fig. 7a) and the preservation of the low-temperature superstructure reflections upon heating to room temperature at 5.5 GPa in our diffraction experiments (Fig. 6e), application of pressure alone does not suffice to induce a transition of Sc_3CoC_4 from the HT to the LT phase structure. No superstructure reflections could be observed in single-crystal XRD experiments up to the destruction of the sample at 10.1 GPa, when the pressure cell was kept constantly at room temperature (see the Supplemental Material⁴³). An overlay of structural models at 0.2 GPa and 4.2 GPa in the Supplemental Material⁴³ illustrates that the pressure-induced shifts of the atomic positions remain negligible under these conditions. Likewise, no phase transition could be inferred from the pressure-dependence of the lattice parameters obtained from room-temperature powder XRD experiments (Fig. 8a). The experimentally observed linear decrease of the lattice parameters upon application of up to 10.1 GPa with a stronger absolute compression of c ($\Delta c = 0.20 \text{ \AA}$) compared to a and b ($\Delta a = 0.07 \text{ \AA}$, $\Delta b = 0.06 \text{ \AA}$) is very well reproduced by DFT studies of the compressibility behavior of the HT phase (Fig. 8a).

This behavior might be related to the strongly differing development of the lattice parameters of Sc_3CoC_4 either upon cooling or upon increasing hydrostatic pressure. Previous variable-temperature neutron diffraction studies between 277 K and 1.8 K showed that a reduction of temperature is accompanied by increases of the b and c parameters by approx. 0.01 Å, and a decrease in the a parameter by approx. 0.02 Å (Fig. 8b).⁸ An increase of hydrostatic pressure, by contrast, results in the compression of all lattice parameters. Thus, a strongly anisotropic pressure response of Sc_3CoC_4 may be suspected in accordance with the low-dimensional structure of the compound. The validity of this hypothesis is underlined by the fact that the application of uniaxial stress along the long axis of single-crystalline Sc_3CoC_4 needles leads to pronounced changes in the temperature-dependent electrical resistivity (see Fig. 4c). We therefore performed a DFT study probing the response of the phonon dispersion to a uniaxial compression along each of the three unit cell axes by varying the HT phase lattice parameters independently (refer to the Supplemental Material⁴³ for further details). The strongest frequency reduction along the W–T phonon branch is obtained by a reduction of the a parameter correlating with the distance between adjacent $[\text{Co}(\text{C}_2)_2]_\infty$ ribbons (see red and blue curves in Fig. 7b). Negative frequencies along the path indicate the instability of the HT phase structure after a compression of the a lattice parameter by more than approx. 0.02 Å. A similar dispersion behavior is only achieved by the application of hydrostatic pressure in the range of 20 GPa.

After pointing out the destabilization of the HT phase under pressure we will now focus on the pressure-induced structural changes to the LT phase. Although the space group $C2/m$ applies to the LT phase structure under ambient-pressure and high-pressure conditions, some degrees of freedom for the atom arrangement remain. We find for example that the distance between adjacent $[\text{Co}(\text{C}_2)_2]_\infty$ ribbons is reduced from 3.378(7) Å at 0 GPa to 3.34(2) Å at 4 GPa. An even smaller compression from 6.0105(3) Å to 5.9849(8) Å is found for the interlayer distance between adjacent quasi-2D Sc1-Co-C layers. Further free parameters in the HT→LT phase transition involve the magnitude of the cobalt and scandium atom shifts, and the extent and relative orientation of the C_2 unit rotations. Fig. 3a and Fig. 3b visualize the effect on the atom positions, when Sc_3CoC_4 is cooled to $T < 40$ K with and without an applied pressure of 4 GPa, respectively. In Fig. 3a the atomic positions at 11 K and ambient pressure are marked by green non-transparent spheres, while Fig. 3b shows the atomic positions after applying a pressure of 4 GPa and cooling to 37 K (orange

non-transparent spheres).

It becomes evident that the general displacement pattern of the cobalt and scandium atoms in the LT phase remains rather invariant upon pressure application: At both 0 GPa and 4 GPa, the cobalt atoms along the $[\text{Co}(\text{C}_2)_2]_\infty$ ribbons are shifted in positive and negative a direction by similar extents of $0.11038(18)$ Å and $0.1125(18)$ Å, respectively. Also the shifts of the Sc1 atoms along the b axis are remarkably similar with values of $0.0574(3)$ Å at 0 GPa and $0.064(2)$ Å at 4 GPa and 37 K. By contrast, the rotation angles of the C_2 units obtained from the structural refinements display a distinct pressure dependency (highlighted in Fig. 3a and Fig. 3b): At 0 GPa and 11 K, the C_2 units are subjected to significant rotations out of their HT phase positions with rotation angles between $5.6(2)^\circ$ and $5.7(2)^\circ$. Nearly vanishing rotation angles of $1(1)^\circ$ are, however, observed at 4 GPa and 37 K (see the Supplemental Material⁴³ for further details). This observation might be linked to the pressure-induced detwinning of Sc_3CoC_4 samples: The two possible twin domains in the ambient-pressure LT phase mainly differ by a different rotation sense of the C_2 units in an otherwise nearly unchanged arrangement of cobalt and scandium atoms. A vanishing C_2 rotation angle makes these twin domains nearly identical leaving only marginal differences in the cobalt and scandium atom positions (further information in the Supplemental Material⁴³). As a result, the realization of a single-domain state extending over the entire sample volume might be favored. The absence of further anomalies in the electrical resistivity between 37 K and the superconducting transition temperature at 4.5 K (Fig. 4b) implies that this detwinned high-pressure low-temperature phase is the one hosting superconductivity in Sc_3CoC_4 .

In a last step we proceed to link the observed temperature- and pressure-dependent changes in the superstructure reflection intensity $I_{\text{XRD}}(T, p)$ (see Fig. 6) to changes observed in the atomic positions. To do so we performed x-ray diffraction experiments at 0 GPa and 4 GPa for selected temperatures above and below the step-like increase of $I_{\text{XRD}}(T, p)$ observed at approx. 80 K and 0 GPa. Fig. 9 gives an overview of the observed temperature-dependence of the Co (blue circles) and Sc1 atom displacements (magenta rectangles) and the C_2 -unit rotations (black triangles) at 0 GPa (a) and 4 GPa (b). Data points from x-ray diffraction experiments with and without usage of a DAC are indicated by filled and open symbols, respectively.

It turns out that the structural models obtained at ambient pressure and above 75 K

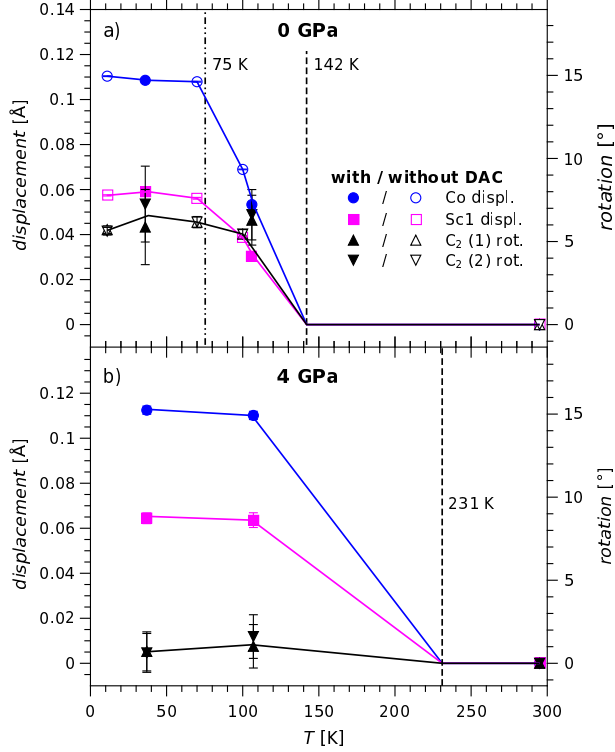


FIG. 9. Temperature-dependence of the displacements of the Co (blue circles) and Sc1 atoms (magenta squares) and the rotation angles of the two symmetry-inequivalent C_2 -units (C_2 (1) and C_2 (2), black triangles) for (a) 0 GPa and (b) 4 GPa. Note that error bars refer to the threefold standard deviation and that the carbon atom displacements corresponding to each C_2 rotation angle (right ordinate) are specified on the left ordinate. Critical temperatures which mark the onset of the formation of superstructure reflections were taken from Fig. 6a and Fig. 6d. In case of the 0 GPa study also the jump-like increase of the superstructure reflection intensity connected to the completion of the Peierls-type transition at 75 K was marked by an additional dotted line. Solid lines serve as guides to the eye.

represent intermediate steps in the progression of Sc_3CoC_4 towards its final state below 75 K (see Fig. 9a). Consistent with the non-zero value of the superstructure reflection intensity in the same temperature- and pressure-regime (Fig. 6a) shifts of the atoms from their positions in the HT phase structure are already present at this stage (Fig. 9a). Thereby, larger values of $I_{XRD}(T, p)$ correspond to larger shifts of the atomic positions. It should be emphasized, however, that the phonon softening process during the HT \rightarrow LT transition is not yet completed for temperatures above 75 K, so that all atom displacements are likely

to be of a correlated, but still dynamical nature.³⁸ When the atom displacements become rather static on cooling below 75 K, a step-like increase and a subsequent saturation of the superstructure reflection intensity is observed.

As already stated above, direction and maximal displacements of the Co and Sc1 atoms are not altered significantly by applying a pressure of 4 GPa. Yet, the absence of a step in $I_{\text{XRD}}(T, p)$ and the higher onset temperature of 231 K (0 GPa: 142 K) correlate with the attainment of these maximum displacements at temperatures significantly above 75 K (see Fig. 9b). The main structural difference between 0 and 4 GPa can thus be attributed to the different extent of the out-of-plane rotation of the C_2 units at all investigated temperatures. Hence, the application of pressure effectively prevents the displacement of the carbon atoms from their HT phase positions, but does not suppress the formation of a periodic structural distortion.

IV. CONCLUSION

To conclude, we suggest a connection between the occurrence of volume superconductivity and subtle structural modifications to the known Peierls-type distorted low-temperature (LT) phase of Sc_3CoC_4 ^{8,3839} under pressure. We demonstrated that the differences between the ambient- and elevated-pressure LT phase structure are limited to a reduction of the C_2 rotations out of the $[\text{Co}(\text{C}_2)_2]_\infty$ ribbon plane from $5.6^\circ - 5.7^\circ$ to nearly zero. This brings the C_2 moieties back to their high-temperature (HT) phase positions in an otherwise still distorted arrangement of cobalt and scandium atoms.

On an atomistic level the changed equilibrium position of the C_2 units may affect phononic and electronic properties of the electron-phonon coupling driven superconductor Sc_3CoC_4 . The importance of carbon atom vibrations for the emergence of superconductivity is highlighted by $^{12}\text{C}/^{13}\text{C}$ isotope substitution experiments indicating a clearly non-zero isotope coefficient of 0.58.⁸⁹ A key role of C_2 librational modes in the coupling of conduction electrons into Cooper pairs is also pointed out by DFT studies employing the Eliashberg formalism.⁹⁰ Thus, establishing structure-property relationships in favor of pressure-induced volume superconductivity presents an interesting, but challenging task for future theoretical studies.

But the subtle changes in the C_2 rotation also affect the properties of Sc_3CoC_4 on a macroscopic level: They render the two possible twin domains in LT- Sc_3CoC_4 nearly indis-

tinguishable and set the stage to the realization of detwinned, single-domain crystals above 1.9 GPa. Thus, a continuous superconducting sample volume may only be realized after the disappearance of twin domain walls from pressurized Sc_3CoC_4 . Such a barrier function of twin domain walls for superconducting currents has been investigated recently by Song *et al.*⁹⁶ for FeSe.

We finally note that our results point to the simultaneous existence of volume superconductivity and a Peierls-type distorted phase at elevated pressures. There seems to be no pressure-adjustable competition between periodic structural distortion and superconductivity like in many other structurally low-dimensional materials.^{16–18,30,86,87} Subtle pressure-induced modifications of the atom arrangement in the distorted phase might already suffice to reconcile both phenomena in Sc_3CoC_4 .

ACKNOWLEDGMENTS

We thank the group of Prof. Ch. Kuntscher for their continuous support in high-pressure studies.

* georg.eickerling@uni-a.de

† wolfgang.scherer@uni-a.de

¹ T. Kim, K. Cho, E. Lee, S. Lee, J. Chae, J. Kim, D. Kim, J. Kwon, G. Amaratunga, S. Lee, B. Choi, Y. Kuk, J. Kim, and K. Kim, *Nature Photon.* **5**, 176 (2011).

² P. Patel, *IEEE Spectr.* **49**, 14 (2012).

³ R. Li, L. Petit, D. Franke, J. Dehollain, J. Helsen, M. Steudtner, N. Thomas, Z. Yoscovits, K. Singh, S. Wehner, L. Vandersypen, J. Clarke, and M. Veldhorst, *Sci. Adv.* **4**, eaar3960 (2018).

⁴ N. Dasgupta, J. Sun, C. Liu, S. Brittman, S. Andrews, J. Lim, H. Gao, R. Yan, and P. Yang, *Adv. Mater.* **26**, 2137 (2014).

⁵ F. Schwierz, *Nature Nanotech.* **5**, 487 (2010).

⁶ G. Hills, C. Lau, A. Wright, S. Fuller, M. Bishop, T. Srimani, P. Kanhaiya, R. Ho, A. Amer, Y. Stein, D. Murphy, Arvind, A. Chandrakasan, and M. Shulaker, *Nature* **572**, 595 (2019).

- ⁷ F. Ando, Y. Miyasaka, T. Li, J. Ishizuka, T. Arakawa, Y. Shiota, T. Moriyama, Y. Yanase, and T. Ono, *Nature* **584**, 373 (2020).
- ⁸ G. Eickerling, C. Hauf, E.-W. Scheidt, L. Reichardt, C. Schneider, A. Muñoz, S. Lopez-Moreno, A. H. Romero, F. Porcher, G. André, R. Pöttgen, and W. Scherer, *Z. Anorg. Allg. Chem.* **639**, 1985 (2013).
- ⁹ W. Little, *Phys. Rev.* **134**, A1416 (1964).
- ¹⁰ W. Little, *Sci. Amer.* **212**, 21 (1965).
- ¹¹ S. Pyon, K. Kudo, and M. Nohara, *J. Phys. Soc. Jpn.* **81**, 053701 (2012).
- ¹² J. Yang, Y. Choi, Y. Oh, A. Hogan, Y. Horibe, K. Kim, B. Min, and S.-W. Cheong, *Phys. Rev. Lett.* **108**, 116402 (2012).
- ¹³ A. Kiswandhi, J. Brooks, H. Cao, J. Yan, D. Mandrus, Z. Jiang, and H. Zhou, *Phys. Rev. B* **87**, 121107 (2013).
- ¹⁴ J. Hodeau, M. Marezio, C. Roucau, R. Ayroles, A. Meerschaut, J. Rouxel, and P. Monceau, *J. Phys. C: Solid State Phys.* **11**, 4117 (1978).
- ¹⁵ M. Regueiro, J.-M. Mignot, and D. Castello, *EPL* **18**, 53 (1992).
- ¹⁶ K. Cho, M. Kończykowski, S. Teknowijoyo, M. Tanatar, J. Guss, P. Gartin, J. Wilde, A. Kreyssig, R. McQueeney, A. Goldman, V. Mishra, P. Hirschfeld, and R. Prozorov, *Nat. Commun.* **9**, 2796 (2018).
- ¹⁷ J. Chang, E. Blackburn, A. Holmes, N. Christensen, J. Larsen, J. Mesot, R. Liang, D. Bonn, W. Hardy, A. Watenphul, M. v. Zimmermann, E. Forgan, and S. Hayden, *Nature Phys.* **8**, 871 (2012).
- ¹⁸ A. Chikina, A. Fedorov, D. Bhoi, V. Voroshnin, E. Haubold, Y. Kushnirenko, K. Kim, and S. Borisenko, *npj Quantum Mater.* **5**, 22 (2020).
- ¹⁹ W. Knafo, F. Duc, F. Bourdarot, K. Kuwahara, H. Nojiri, D. Aoki, J. Billette, P. Frings, X. Tonon, E. Lelièvre-Berna, J. Flouquet, and L.-P. Regnault, *Nat. Commun.* **7**, 13075 (2016).
- ²⁰ A. V. Chubukov, D. V. Efremov, and I. Eremin, *Phys. Rev. B* **78**, 134512 (2008).
- ²¹ P. Dai, J. Hu, and E. Dagotto, *Nature Phys.* **8**, 709 (2012).
- ²² A. Meerschaut and J. Rouxel, *J. Less-Common Met.* **39**, 197 (1975).
- ²³ L. Yang, Y. Tao, J. Liu, C. Liu, Q. Zhang, M. Akter, Y. Zhao, T. Xu, Y. Xu, Z. Mao, Y. Chen, and D. Li, *Nano Lett.* **19**, 415 (2019).
- ²⁴ K. Novoselov, A. Geim, S. Morozov, D. Jiang, Y. Zhang, S. Dubonos, I. Grigorieva, and

- A. Firsov, *Science* **306**, 666 (2004).
- ²⁵ Y. Cao, V. Fatemi, S. Fang, K. Watanabe, T. Taniguchi, E. Kaxiras, and P. Jarillo-Herrero, *Nature* **556**, 43 (2018).
- ²⁶ P. Williams, G. Parry, and C. Scrub, *Phil. Mag.* **29**, 695 (1974).
- ²⁷ S.-H. Lee, J. Goh, and D. Cho, *Phys. Rev. Lett.* **122**, 106404 (2019).
- ²⁸ H. Hughes, *J. Phys. C: Solid State Phys.* **10**, L319 (1977).
- ²⁹ G.-J. Shu, Y. Zhou, M.-Y. Kao, C. Klingshirn, M. Huang, Y.-L. Huang, Y. Liang, W. Kuo, and S.-C. Liou, *Appl. Phys. Lett.* **114**, 202103 (2019).
- ³⁰ H. Oike, M. Kamitani, Y. Tokura, and F. Kagawa, *Sci. Adv.* **4**, eaau3489 (2018).
- ³¹ B. Rohmoser, G. Eickerling, M. Presnitz, W. Scherer, V. Eyert, R.-D. Hoffmann, U. Rodewald, C. Vogt, and R. Pöttgen, *J. Am. Chem. Soc.* **129**, 9356 (2007).
- ³² W. Jeitschko, M. Gerss, R.-D. Hoffmann, and S. Lee, *J. Less-Common Met.* **156**, 397 (1989).
- ³³ A. Tsokol', O. Bodak, and E. Marusin, *Sov. Phys. Crystallogr.* **31**, 466 (1986).
- ³⁴ W. Scherer, C. Hauf, M. Presnitz, E.-W. Scheidt, G. Eickerling, V. Eyert, R.-D. Hoffmann, U. C. Rodewald, A. Hammerschmidt, C. Vogt, and R. Pöttgen, *Angew. Chem. Int. Ed.* **49**, 1578 (2010).
- ³⁵ E.-W. Scheidt, C. Hauf, F. Reiner, G. Eickerling, and W. Scherer, *J. Phys.: Conf. Ser.* **273**, 012083 (2011).
- ³⁶ W. Scherer, G. Eickerling, C. Hauf, M. Presnitz, E.-W. Scheidt, V. Eyert, and R. Pöttgen, *Modern Charge-Density Analysis*, 1st ed., edited by C. Gatti and P. Macchi (Springer Netherlands, 2012) Chap. 10, pp. 359–385.
- ³⁷ M. He, C. Wong, D. Shi, P. Tse, E.-W. Scheidt, G. Eickerling, W. Scherer, P. Sheng, and R. Lortz, *J. Phys.: Condens. Matter* **27**, 075702 (2015).
- ³⁸ J. Langmann, C. Haas, E. Wenger, D. Schaniel, W. Scherer, and G. Eickerling, *Phys. Rev. B* **102**, 094109 (2020).
- ³⁹ E. Wang, X. Zhu, and H.-W. Wen, *EPL* **115**, 27007 (2016).
- ⁴⁰ C. Vogt, R.-D. Hoffmann, U. Rodewald, G. Eickerling, M. Presnitz, V. Eyert, W. Scherer, and R. Pöttgen, *Inorg. Chem.* **48**, 6436 (2009).
- ⁴¹ A. Jesche and P. Canfield, *Philos. Mag.* **94**, 2372 (2014).
- ⁴² C. Haas, *Strukturelle und physikalische Charakterisierungen niederdimensionaler Metallborocarbide und Metallcarbide*, Ph.D. thesis, University of Augsburg (2019).

- ⁴³ See Supplemental Material at [URL will be inserted by publisher] for information on synthesis and properties of the investigated samples, details of the magnetization, resistivity and x-ray diffraction experiments under ambient and high-pressure conditions, phonon dispersion relations under uniaxial strain, and remarks on the analysis of the experimental data.
- ⁴⁴ N. Tateiwa, Y. Haga, T. Matsuda, and Z. Fisk, *J. Phys.: Conf. Ser.* **500**, 142032 (2014).
- ⁴⁵ N. Tateiwa, Y. Haga, T. Matsuda, Z. Fisk, S. Ikeda, and H. Kobayashi, *Rev. Sci. Instrum.* **84**, 046105 (2013).
- ⁴⁶ N. Tateiwa, Y. Haga, T. Matsuda, and Z. Fisk, *Rev. Sci. Instrum.* **83**, 053906 (2012).
- ⁴⁷ N. Tateiwa, Y. Haga, Z. Fisk, and Y. Ōnuki, *Rev. Sci. Instrum.* **82**, 053906 (2011).
- ⁴⁸ T. Kobayashi, H. Hidaka, H. Kotegawa, K. Fujiwara, and M. Eremets, *Rev. Sci. Instrum.* **78**, 023909 (2007).
- ⁴⁹ A. Eiling and J. Schilling, *J. Phys. F: Met. Phys.* **11**, 623 (1981).
- ⁵⁰ B. Bireckoven and J. Wittig, *J. Phys. E: Sci. Instrum.* **21**, 841 (1988).
- ⁵¹ K. Yokogawa, K. Murata, H. Yoshino, and S. Aoyama, *Jpn. J. Appl. Phys.* **46**, 3636 (2007).
- ⁵² K. Murata, K. Yokogawa, H. Yoshino, S. Klotz, P. Munsch, A. Irizawa, M. Nishiyama, K. Iizuka, T. Nanba, T. Okada, Y. Shiraga, and S. Aoyama, *Rev. Sci. Instrum.* **79**, 085101 (2008).
- ⁵³ M. Nicklas, “Pressure probes” in *Strongly Correlated Systems: Experimental Techniques*, edited by A. Avella and F. Mancini (Springer Berlin Heidelberg, Berlin, Heidelberg, 2015) Chap. 6, pp. 173–204.
- ⁵⁴ D. Schmitz, *Experimentelle Hochdruckstudien an metallorganischen Modellsystemen mit aktivierten Kohlenstoff-Wasserstoff oder Silizium-Wasserstoff Bindungen*, Ph.D. thesis, University of Augsburg (2018).
- ⁵⁵ A. Le Bail, H. Duroy, and J. Fourquet, *Mater. Res. Bull.* **23**, 447 (1988).
- ⁵⁶ J.-F. Bérar and P. Lelann, *J. Appl. Cryst.* **24**, 1 (1991).
- ⁵⁷ V. Petříček, M. Dušek, and L. Palatinus, *Z. Kristallogr.* **229**, 345 (2014).
- ⁵⁸ P. Willmott, D. Meister, S. Leake, M. Lange, A. Bergamaschi, M. Böge, M. Calvi, C. Cancellieri, N. Casati, A. Cervellino, Q. Chen, C. David, U. Flechsig, F. Gozzo, B. Henrich, S. Jäggi-Spielmann, B. Jakob, I. Kalichava, P. Karvinen, J. Krempasky, A. Lüdeke, R. Lüscher, S. Maag, C. Quitmann, M. Reinle-Schmitt, T. Schmidt, B. Schmitt, A. Streun, I. Vartiainen, M. Vitins, X. Wang, and R. Wulschleger, *J. Synchrotron Rad.* **20**, 667 (2013).

- ⁵⁹ M. Fisch, A. Lanza, P. Macchi, and N. Casati, *J. Appl. Cryst.* **48**, 1956 (2015).
- ⁶⁰ A. Bergamaschi, A. Cervellino, R. Dinapoli, F. Gozzo, B. Henrich, I. Johnson, P. Kraft, A. Mozanica, B. Schmitt, and X. Shi, *J. Synchrotron Rad.* **17**, 653 (2010).
- ⁶¹ G. Piermarini, S. Block, and J. Barnett, *J. Appl. Phys.* **44**, 5377 (1973).
- ⁶² R. Angel, D. Allan, R. Miletich, and L. Finger, *J. Appl. Cryst.* **30**, 461 (1997).
- ⁶³ D. Graf, R. Stillwell, K. Purcell, and S. Tozer, *High Pressure Res.* **31**, 533 (2011).
- ⁶⁴ R. Boehler and K. De Hantsetters, *High Pressure Res.* **24**, 391 (2004).
- ⁶⁵ K. Murata and S. Aoki, *Rev. High Pressure Sci. Technol.* **26**, 3 (2016).
- ⁶⁶ G. Piermarini, S. Block, J. Barnett, and R. Forman, *J. Appl. Phys.* **46**, 2774 (1975).
- ⁶⁷ A. Dewaele, M. Torrent, P. Loubeyre, and M. Mezouar, *Phys. Rev. B* **78**, 104102 (2008).
- ⁶⁸ I. Kantor, “Fluorescence pressure calculation and thermocouple tools,” [online; accessed 14-December-2020].
- ⁶⁹ R. Boehler, *Rev. Sci. Instrum.* **77**, 115103 (2006).
- ⁷⁰ A. Duisenberg, *J. Appl. Cryst.* **25**, 92 (1992).
- ⁷¹ A. Duisenberg, L. Kroon-Batenburg, and A. Schreurs, *J. Appl. Cryst.* **36**, 220 (2003).
- ⁷² L. Krause, R. Herbst-Irmer, G. Sheldrick, and D. Stalke, *J. Appl. Cryst.* **48**, 3 (2015).
- ⁷³ G. Kresse and J. Furthmüller, *Comput. Mater. Sci.* **6**, 15 (1996).
- ⁷⁴ G. Kresse and J. Furthmüller, *Phys. Rev. B* **54**, 11169 (1996).
- ⁷⁵ G. Kresse and J. Hafner, *Phys. Rev. B* **49**, 14251 (1994).
- ⁷⁶ G. Kresse and J. Hafner, *Phys. Rev. B* **47**, 558 (1993).
- ⁷⁷ J. Perdew, K. Burke, and M. Ernzerhof, *Phys. Rev. Lett.* **77**, 3865 (1996).
- ⁷⁸ J. Perdew, K. Burke, and M. Ernzerhof, *Phys. Rev. Lett.* **78**, 1396 (1997).
- ⁷⁹ A. Togo and I. Tanaka, *Scr. Mater.* **108**, 1 (2015).
- ⁸⁰ F. Brown, *Structural Phase Transitions in Layered Transition Metal Compounds*, edited by K. Motizuki, *Physics and Chemistry of Materials with Low-Dimensional Structures*, Vol. 8 (Springer Netherlands, 1986) Chap. 4, pp. 267–292.
- ⁸¹ Y. Joe, X. Chen, P. Ghaemi, K. Finkelstein, G. de La Peña, Y. Gan, J. Lee, S. Yuan, J. Geck, G. MacDougall, T. Chiang, S. Cooper, E. Fradkin, and P. Abbamonte, *Nature Phys.* **10**, 421 (2014).
- ⁸² N. Wakabayashi, H. Smith, K. Woo, and F. Brown, *Solid State Commun.* **28**, 923 (1978).
- ⁸³ D. Moncton, J. Axe, and F. DiSalvo, *Phys. Rev. Lett.* **34**, 734 (1975).

- ⁸⁴ D. Moncton, J. Axe, and F. DiSalvo, Phys. Rev. B **16**, 801 (1977).
- ⁸⁵ A. Kusmartseva, B. Sipos, H. Berger, L. Forro, and E. Tutiš, Phys. Rev. Lett. **103**, 236401 (2009).
- ⁸⁶ D. Freitas, P. Rodière, M. Osorio, E. Navarro-Moratalla, N. Nemes, V. Tissen, L. Cario, E. Coronado, M. García-Hernández, S. Vieira, M. Núñez-Regueiro, and H. Suderow, Phys. Rev. B **93**, 184512 (2016).
- ⁸⁷ C. Berthier, P. Molinié, and D. Jérôme, Solid State Commun. **18**, 1393 (1976).
- ⁸⁸ Y. Feng, J. Wang, R. Jaramillo, J. Van Wezel, S. Haravifard, G. Srajer, Y. Liu, Z.-A. Xu, P. Littlewood, and T. Rosenbaum, PNAS **109**, 7224 (2012).
- ⁸⁹ C. D. Haas, G. Eickerling, E.-W. Scheidt, D. Schmitz, J. Langmann, J. Lyu, J. Shen, R. Lortz, D. Eklöf, J. G. Schiffmann, L. van Wüllen, A. Jesche, and W. Scherer, arXiv:1712.05649v3 (2017).
- ⁹⁰ C. Zhang, J. Tse, K. Tanaka, and H.-Q. Lin, EPL **100**, 67003 (2012).
- ⁹¹ This twinning process is due to a $t2$ step followed by an $i2$ step in the symmetry reduction (*translationengliche* and isomorphic group-subgroup relationship, respectively) from the space-group $Immm$ of the HT phase structure to the space-group $C2/m$ of the LT phase structure, see Refs. 8 and 40.
- ⁹² We note that a preference for one of the twin domains emerges well below the quasi-hydrostatic limit of the employed pressure transmitting medium (Daphne 7575) at 3.9 GPa - 4 GPa ($T = 298$ K, see Ref. 65) in contrast to the usually required uni-directional pressures in other reported examples of detwinning (see Refs. 97, 98, and 99). Solidification of the pressure medium upon cooling does not induce significant non-hydrostaticity, as demonstrated in Ref. 100.
- ⁹³ L. Zhang, C. Fehse, H. Eckert, C. Vogt, R.-D. Hoffmann, and R. Pöttgen, Solid State Sci. **9**, 699 (2007).
- ⁹⁴ C. Vogt, R.-D. Hoffmann, and R. Pöttgen, Solid State Sci. **7**, 1003 (2005).
- ⁹⁵ The fact that the calculations do not predict a preferential phonon frequency reduction at T may be related to shortcomings of the standard GGA functional employed within this study to properly resolve the very flat energy surface region separating the HT and LT phase of Sc_3CoC_4 .
- ⁹⁶ C.-L. Song, Y.-L. Wang, Y.-P. Jiang, L. Wang, K. He, X. Chen, J. Hoffman, X.-C. Ma, and Q.-K. Xue, Phys. Rev. Lett. **109**, 137004 (2012).

- ⁹⁷ K. Grube, W. Fietz, U. Tutsch, O. Stockert, and H. v. Löhneysen, Phys. Rev. B **60**, 11947 (1999).
- ⁹⁸ F. Gugenberger, C. Meingast, G. Roth, K. Grube, V. Breit, T. Weber, H. Wühl, S. Uchida, and Y. Nakamura, Phys. Rev. B **49**, 13137 (1994).
- ⁹⁹ S. Niesen, G. Kolland, M. Seher, O. Breunig, M. Valldor, M. Braden, B. Grenier, and T. Lorenz, Phys. Rev. B **87**, 224413 (2013).
- ¹⁰⁰ D. Staško, J. Prchal, M. Klicpera, S. Aoki, and K. Murata, High. Press. Res. **40**, 525 (2020).

Supplemental Material for: The structure of the superconducting high-pressure phase of Sc_3CoC_4

Jan Langmann,¹ Marcel Vöst,¹ Dominik Schmitz,¹ Christof Haas,¹

Georg Eickerling,^{1,*} Anton Jesche,² Michael Nicklas,³ Arianna

Lanza,⁴ Nicola Casati,⁵ Piero Macchi,⁶ and Wolfgang Scherer^{1,†}

¹*CPM, Institut für Physik, Universität Augsburg, D-86159 Augsburg, Germany*

²*Experimentalphysik VI, Zentrum für Elektronische Korrelation und Magnetismus,
Institut für Physik, Universität Augsburg, D-86159 Augsburg, Germany*

³*Max Planck Institute for Chemical Physics of Solids,
Nöthnitzer Straße 40, D-01087 Dresden, Germany*

⁴*Center for Nanotechnology Innovation@NEST,
Istituto Italiano di Tecnologia, I-56127 Pisa, Italy*

⁵*Swiss Light Source, Paul Scherrer Institut, CH-5232 Villigen, Switzerland*

⁶*Dipartimento di Chimica, Materiali ed Ingegneria Chimica “G. Natta”,
Politecnico di Milano, I-20133 Milano, Italy*

(Dated: December 31, 2021)

CONTENTS

I. Synthesis of samples	3
II. Investigated samples	4
III. High-pressure magnetization measurements	6
IV. High-pressure electrical resistivity measurements	9
V. High-pressure powder x-ray diffraction studies	11
VI. Single-crystal x-ray diffraction experiments	16
A. Data collection and reduction	16
B. Overview of experiments	19
C. Ambient-pressure low-temperature measurements without pressure cell	21
D. High-pressure low-temperature measurements	24
E. Superstructure reflections at room temperature	26
F. Test for sample degradation in high-pressure/low-temperature studies	29
G. High-pressure measurements at room temperature	32
VII. Phonon dispersion relations under uniaxial strain	35
VIII. Analysis of experimental data	36
A. Calculation of atom displacements	36
B. Sensitivity of superstructure reflection intensities to atom displacements	39
C. Reliability of the refined atom displacements	41
D. Differences between twin domains	49
References	50

I. SYNTHESIS OF SAMPLES

All Sc_3CoC_4 single crystals in this work were grown from polycrystalline samples. These were obtained by arc-melting pieces of the constituent elements scandium (Smart Elements, 5N), cobalt (Cerametec Materials, 5N5) and carbon (Alfa Aesar, 5N5) in a purified argon atmosphere (500 mbar). Homogeneity was ensured by re-melting the sample several times (see also Refs. 1 and 2).

Single-crystalline needles of Sc_3CoC_4 (see Fig. S2) develop spontaneously at the surface of polycrystalline samples after rapid quenching from high temperatures in the arc-melting furnace. Thereby, a large temperature gradient from sample top to bottom is achieved using a water-cooled copper crucible (see also Refs. 3 and 4).

Larger plate-like single crystals (see Fig. S1, Fig. S3 and Fig. S4) were grown by crystallization from a lithium flux.⁵ For this purpose, powder from a ground polycrystalline sample of Sc_3CoC_4 and small lithium pieces (Alfa Aesar, 3N) were filled into a tantalum ampoule in a stoichiometric ratio of 1:20. The tantalum ampoule was closed by welding under argon atmosphere (500 mbar), sealed into an evacuated quartz ampoule and placed in a muffle furnace. After heating to 600 °C with a heating rate of 20 °C/h the temperature was held constant for 24 hours and then reduced to 500 °C with a cooling rate of 100 °C/h. The heat treatment was terminated after two to four weeks by quenching the samples in a water bath. Single crystals were obtained by opening and turning the tantalum ampoule under inert conditions. Remaining flux medium was dissolved in ethanol (see also Ref. 4).

II. INVESTIGATED SAMPLES

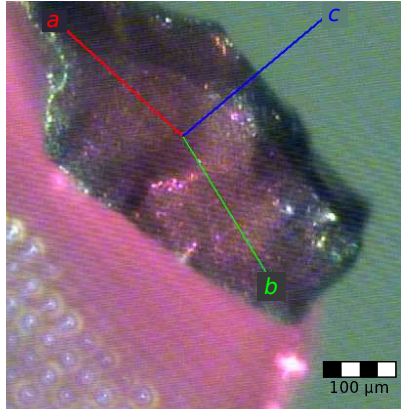


FIG. S1. Photographic image of the single-crystalline Sc_3CoC_4 sample used in the high-pressure magnetization measurements. Crystal axes a , b and c referring to the orthorhombic high-temperature phase unit cell are indicated by colored lines.

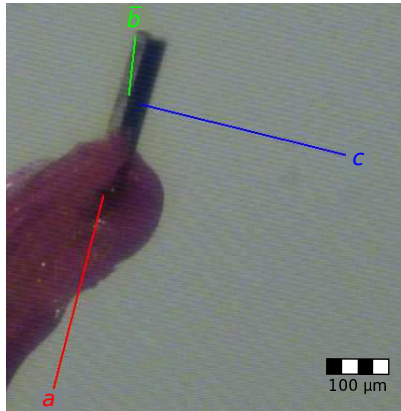


FIG. S2. Photographic image of the Sc_3CoC_4 single crystal used in the ambient-pressure low-temperature x-ray diffraction experiments without pressure cell. Crystal axes a , b and c referring to the orthorhombic high-temperature phase unit cell are indicated by colored lines.

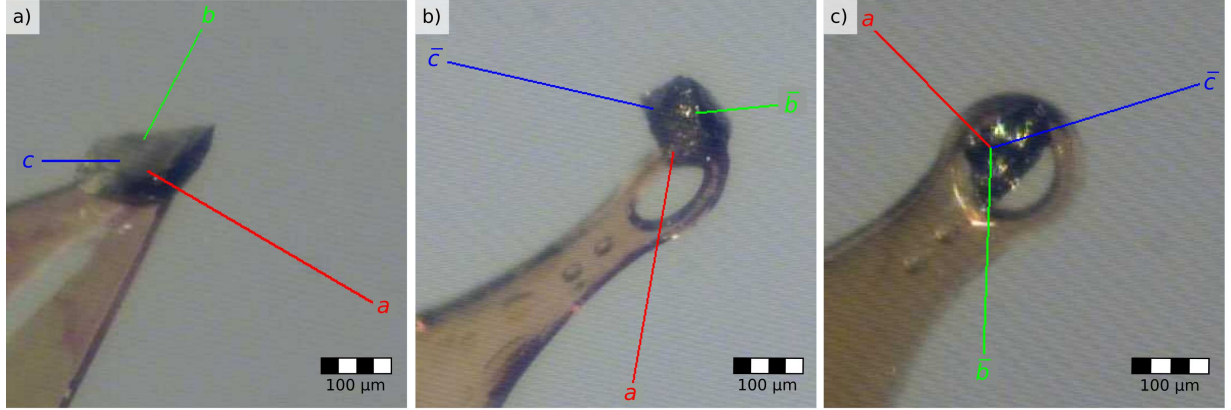


FIG. S3. Photographic images of the Sc_3CoC_4 single crystals used in the high-pressure low-temperature x-ray diffraction experiments for (a) tracking of superstructure reflection intensities, (b) structure determinations, and (c) tests for sample degradation under the high-pressure/low-temperature conditions. Crystal axes a , b and c referring to the orthorhombic high-temperature phase unit cell are indicated by colored lines.

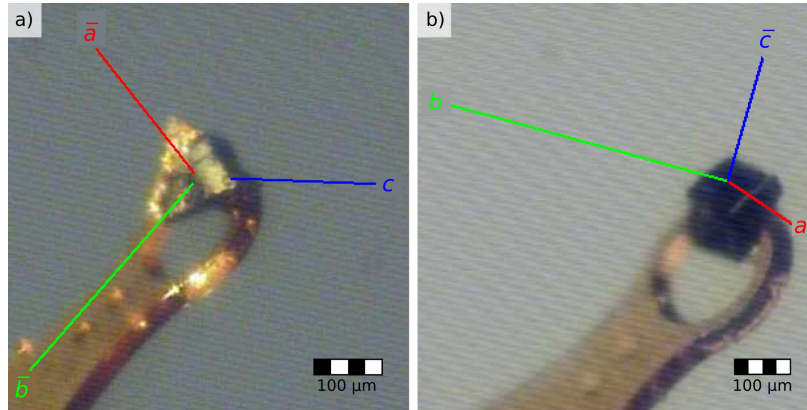


FIG. S4. Photographic images of the Sc_3CoC_4 single crystals used in the high-pressure x-ray diffraction experiments at room temperature for (a) structure determination, and (b) reciprocal space mapping. Crystal axes a , b and c referring to the orthorhombic high-temperature phase unit cell are indicated by colored lines.

III. HIGH-PRESSURE MAGNETIZATION MEASUREMENTS

For performing high-pressure magnetization measurements a miniature Ceramic Anvil Cell (mCAC)⁶⁻¹⁰ was used. The ceramic anvils had a culet diameter of 1.8 mm and the prefabricated Cu:Be gasket had a pressure chamber diameter of 900 μm and a thickness of 900 μm . Placing a piece of lead inside the pressure chamber allowed to infer the internal pressure from its superconducting transition temperature T_c .^{11,12} As pressure transmitting medium served Daphne 7373 with a quasi-hydrostatic limit of 2.2 GPa - 2.3 GPa.^{13,14} After a background measurement of the closed mCAC with a piece of lead (dimensions: 105 $\mu\text{m} \times 255 \mu\text{m} \times 300 \mu\text{m}$) and Daphne 7373 inside its pressure chamber (orange triangles in Fig. S5 and Fig. S6) the actual sample measurement with an additional Sc_3CoC_4 single crystal (dimensions: 225 $\mu\text{m} \times 270 \mu\text{m} \times 600 \mu\text{m}$; mass: 69.2 μg ; photographic image in Fig. S1) at pressures of 0.11 GPa, 1.18 GPa, 1.45 GPa, 1.48 GPa and 0.19 GPa (pressure release measurement) took place (see Fig. S5 and Fig. S6 for an overview of the raw data collected upon increasing and decreasing the applied pressure, respectively). Reciprocal space planes reconstructed from x-ray diffraction data collected before and after the high-pressure study can be found in Fig. S7. As comparative measurements serve magnetization measurements, where the same Sc_3CoC_4 single crystal was fixed on a glass rod with GE Varnish before (cyan diamonds in Fig. S5) and after the high-pressure study (violet triangles in Fig. S6). All magnetization measurements were performed under zero-field-cooling conditions employing a MPMS3 superconducting quantum interference device (SQUID) magnetometer (QUANTUM DESIGN). The measured temperature range was between 1.8 K and 9 K with a heating rate of 0.2 K/min at 5 Oe. For analyzing the data, the background measurement was in each case subtracted.

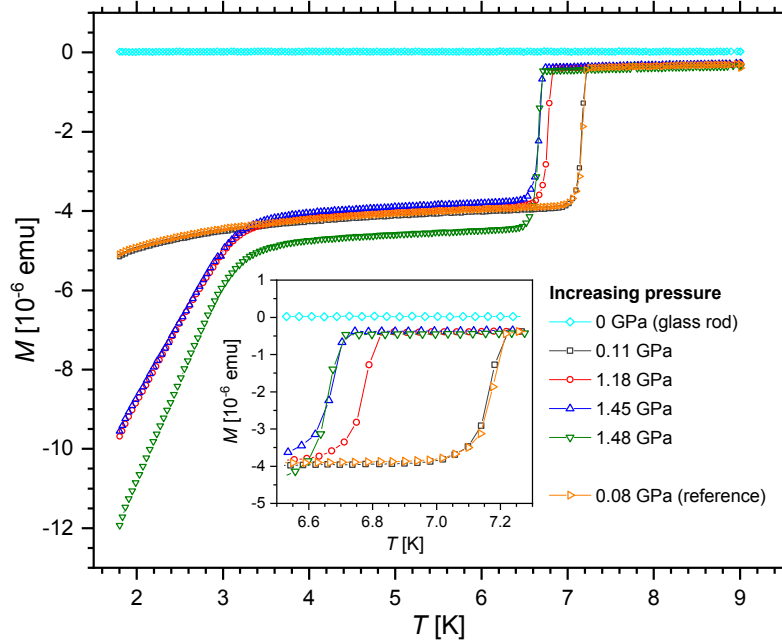


FIG. S5. Unprocessed magnetization data $M(T)$ collected with increasing pressure. Data points of a reference measurement with only a lead piece and pressure-transmitting medium inside the pressure chamber are plotted with orange triangles.

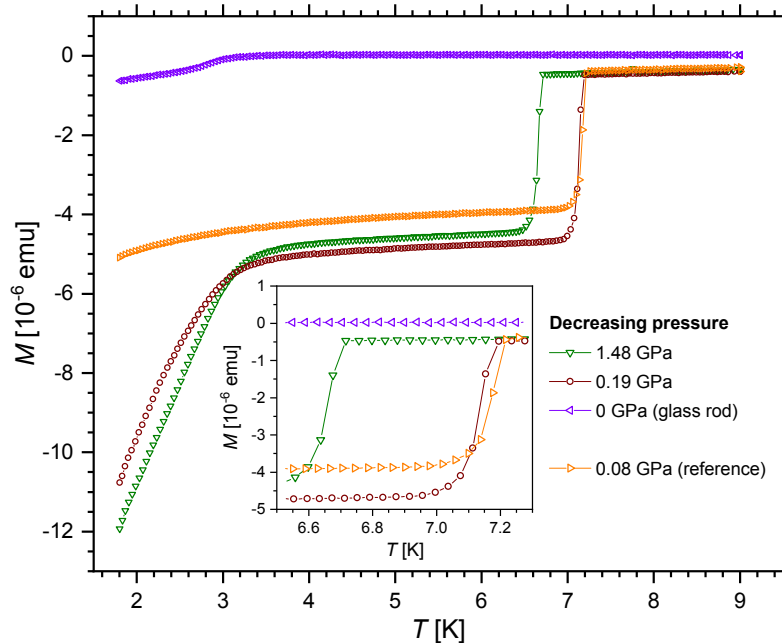


FIG. S6. Unprocessed magnetization data $M(T)$ collected with decreasing pressure. Data points of a reference measurement with only a lead piece and pressure-transmitting medium inside the pressure chamber are plotted with orange triangles.

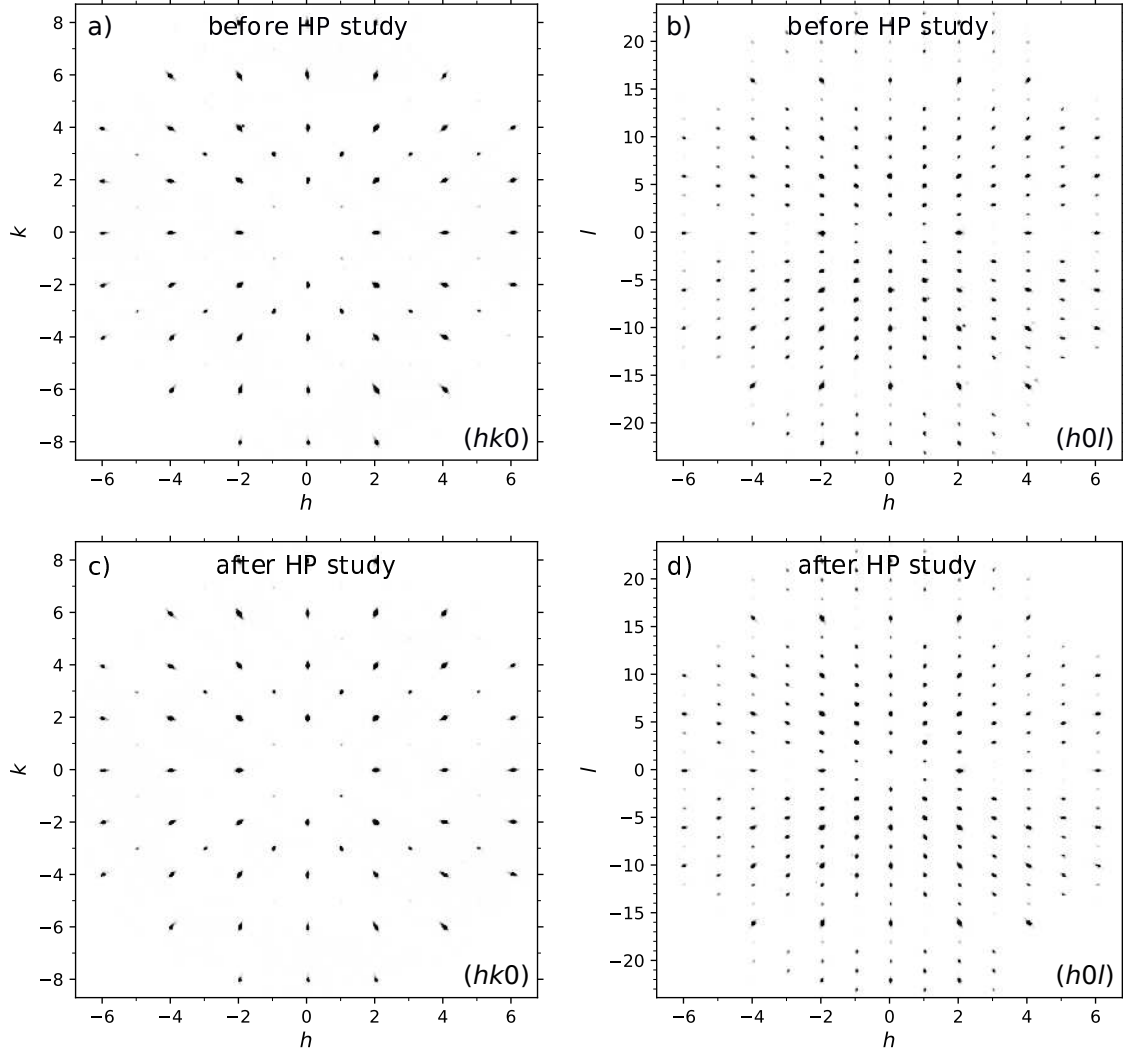


FIG. S7. Reconstructions of reciprocal-space planes $(hk0)$ and $(h0l)$ from room-temperature x-ray diffraction data collected for a Sc_3CoC_4 single crystal before (a, b) and after performing a high-pressure magnetization study on it (c, d).

IV. HIGH-PRESSURE ELECTRICAL RESISTIVITY MEASUREMENTS

For high-pressure electrical resistivity measurements a nonmagnetic piston-cylinder-type pressure cell was used.¹⁵ By using silver conductive paint a crystalline Sc_3CoC_4 whisker (dimensions: $15\ \mu\text{m} \times 35\ \mu\text{m} \times 2740\ \mu\text{m}$) was four-point contacted *via* gold filaments which were attached to copper wires. Beforehand and in order to stabilize this setup, the whisker was at one side slightly fixed to a mica plate employing GE-7031 varnish. On the backside of this mica plate a lead platelet was attached, which itself was connected *via* the four-point method and served as pressure manometer. A silicon oil was utilized as pressure-transmitting medium inside the Teflon cap of the high-pressure cell. For determining the resistivity a LINEAR RESEARCH LR700 resistance bridge was used. In order to cool the high-pressure cell setup from 300 K to 1.8 K the cryostat function of a physical property measurement system (PPMS; QUANTUM DESIGN) was employed. Monitoring the temperature of the high-pressure cell was possible by a thermometer (LAKE SHORE) fixed inside the shell of the pressure cell. For each pressure point the resistivity was measured during the cooling process to 1.8 K. After that the pressure was determined by fine-sliced resistivity measurements in a temperature range of 0.3 K around the superconducting transition temperature of Pb.^{11,12} Lastly followed the resistivity measurement while heating the setup from 1.8 K to 300 K.¹⁶ The unprocessed resistivity data for pressures of 0.03 GPa and 0.82 GPa is given in Fig. S8.

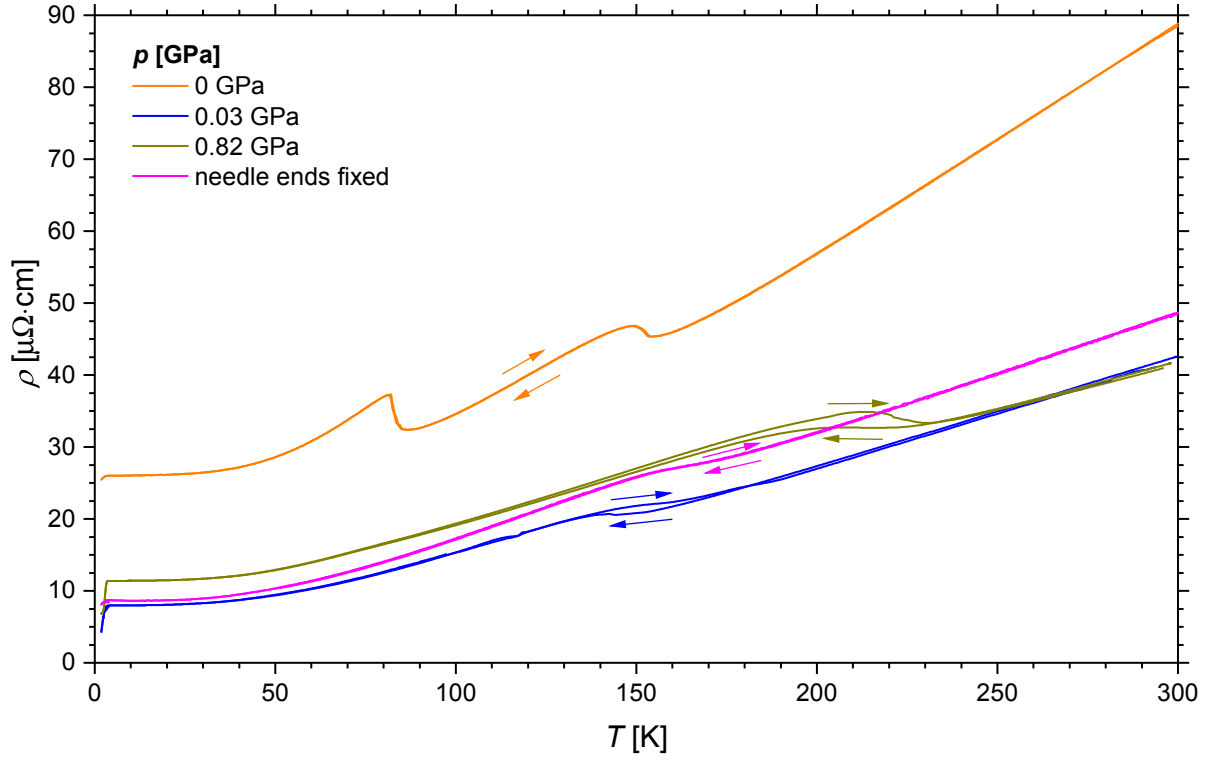


FIG. S8. Unprocessed electrical resistivity data $\rho(T)$ for the measurements under hydrostatic pressures of 0.03 GPa (blue) and 0.82 GPa (dark yellow). For comparison, $\rho(T)$ is also given for measurements under ambient pressure (orange) and uniaxial stress (magenta) that were performed on different samples.

V. HIGH-PRESSURE POWDER X-RAY DIFFRACTION STUDIES

High-pressure powder x-ray diffraction experiments were performed at the X04SA Materials Science (MS) beamline at Swiss Light Source (SLS)^{17,18} employing a primary beam energy of 25 keV and a PSI Mythen II one-dimensional detector.¹⁹ A radiation wave length of 0.49573 Å was determined from the LaB₆ cell parameters refined for an initial calibration measurement on a NIST SRM 660a powder standard.

Pressures up to 10.29(4) GPa were generated by a diamond anvil cell (DAC) equipped with 0.5 mm wide culets and stainless steel gaskets providing a pressure chamber with 200 μm diameter and 45 μm - 60 μm thickness. The pressure cell was loaded with finely ground and sieved Sc₃CoC₄ powder (nominal sieve opening 32 μm) and a 4:1 MeOH:EtOH volume mixture serving as a pressure-transmitting medium.²⁰ Powdered α-quartz was added as an internal pressure gauge exploiting the well-established compression behavior of its lattice parameters.²¹ With the exception of the DAC filling process all sample preparation steps were performed under an inert argon atmosphere to prevent a potential sample degradation.

During data collection the pressure cell was oscillated continuously by ±3° around the ω axis, *i.e.* perpendicular to the primary beam,¹⁸ to bring a large number of differently oriented crystallites into diffracting position. Remote operation of the DAC by a helium-gas-driven membrane system allowed to change the pressure while maintaining a consistent sample orientation.

Exemplary powder x-ray diffraction patterns obtained at pressures of 0 GPa, 9.15(4) GPa, and 10.29(4) GPa (see Fig. S9, Fig. S10, and Fig. S11) illustrate the absence of additional reflections within the investigated pressure range between 0 GPa and 10.29(4) GPa. Only a simultaneous broadening of the reflection profiles for Sc₃CoC₄ and α-quartz is observed for pressures above 9.15(4) GPa (Fig. S11) pointing to an incipient non-hydrostaticity of the employed pressure medium (quasi-hydrostatic limit ≈10 GPa²⁰). Thus, all observed reflections can be attributed to Sc₃CoC₄ in its high-temperature phase (space group *Immm*), the pressure calibrant α-quartz or parasitic scattering from the surroundings of the pressure chamber, *i.e.* from the DAC body including the gasket and the diamonds. In Le Bail fits²² of the diffraction data with the program JANA2006²³ the latter reflections were added to the background description (specified by 100 points), whereas Sc₃CoC₄ and α-quartz reflections in the 2θ range between 3° and 30° were modelled by purely Lorentzian profiles (fit lines

and difference plots at selected pressure can be found in Fig. S9 to Fig. S11, an overview of profile Rp factors and lattice parameters is available in Tab. I). Standard deviations of the refined lattice parameters are specified with applied Berar's correction²⁴ as implemented in JANA2006.²³

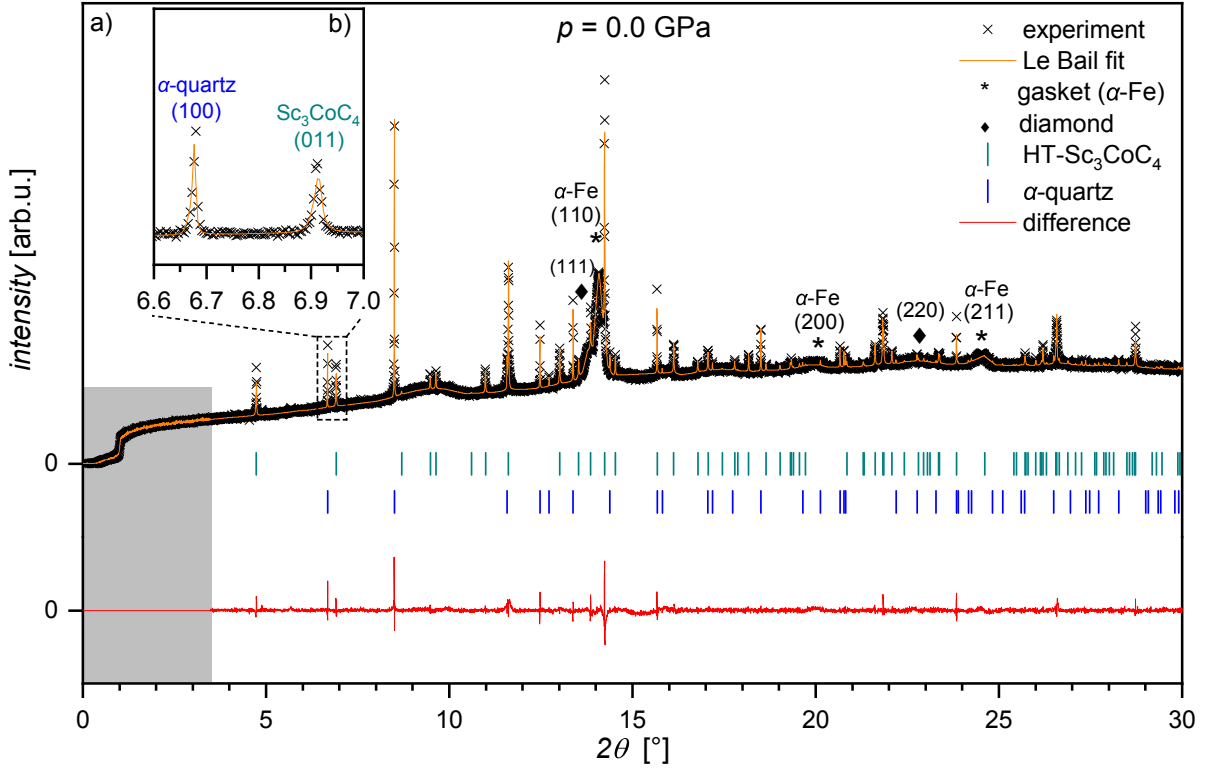


FIG. S9. (a) Room-temperature powder x-ray diffraction pattern (black crosses), Le Bail fit (orange line) and according difference plot (red line) for a Sc_3CoC_4 sample at a pressure of 0.0 GPa ($\lambda = 0.49573 \text{ \AA}$). Expected reflection positions for Sc_3CoC_4 in its high-temperature phase and α -quartz are indicated by green and blue bars, respectively. Asterisks and diamonds mark the positions of parasitic reflections from the gasket and the pressure-cell diamonds, while regions excluded from the Le Bail fit are shaded in gray. (b) Enlarged view of the (011) reflection for Sc_3CoC_4 and the (100) reflection for α -quartz.

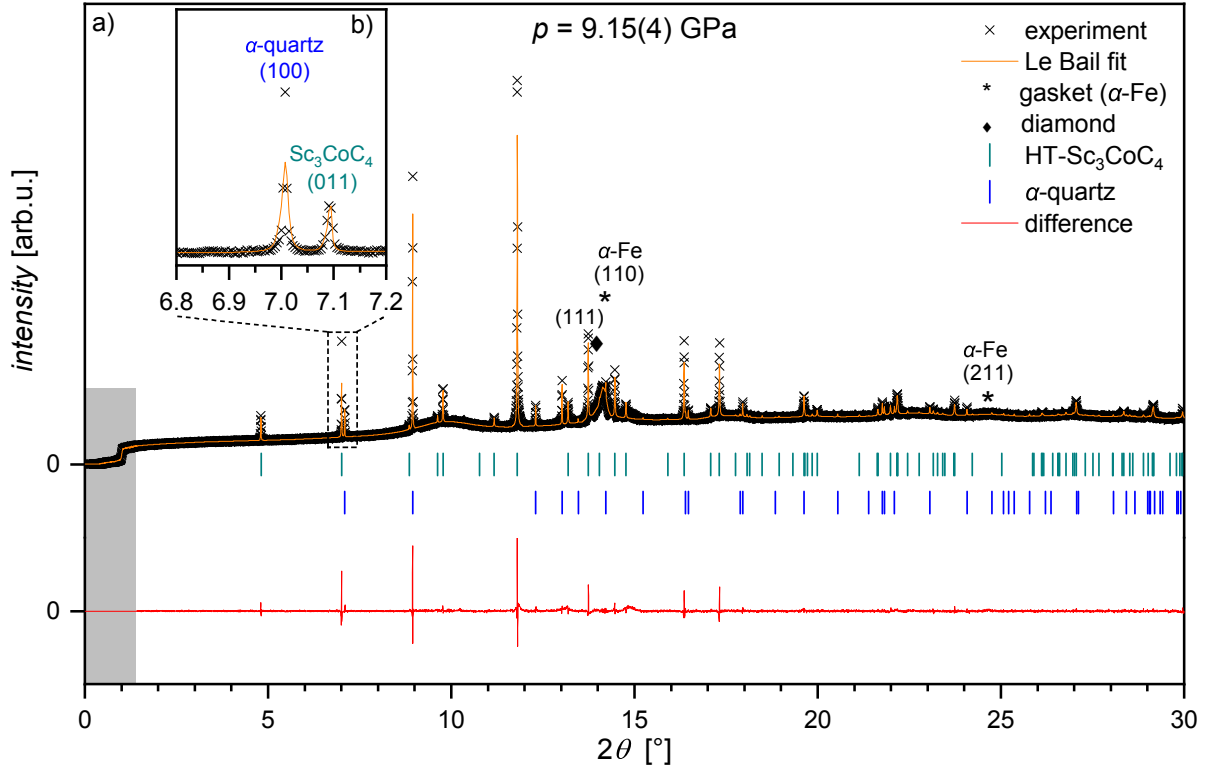


FIG. S10. (a) Room-temperature powder x-ray diffraction pattern (black crosses), Le Bail fit (orange line) and according difference plot (red line) for a Sc_3CoC_4 sample at a pressure of 9.15(4) GPa ($\lambda = 0.49573$ Å). Expected reflection positions for Sc_3CoC_4 in its high-temperature phase and α -quartz are indicated by green and blue bars, respectively. Asterisks and diamonds mark the positions of parasitic reflections from the gasket and the pressure-cell diamonds, while regions excluded from the Le Bail fit are shaded in gray. (b) Enlarged view of the (011) reflection for Sc_3CoC_4 and the (100) reflection for α -quartz.

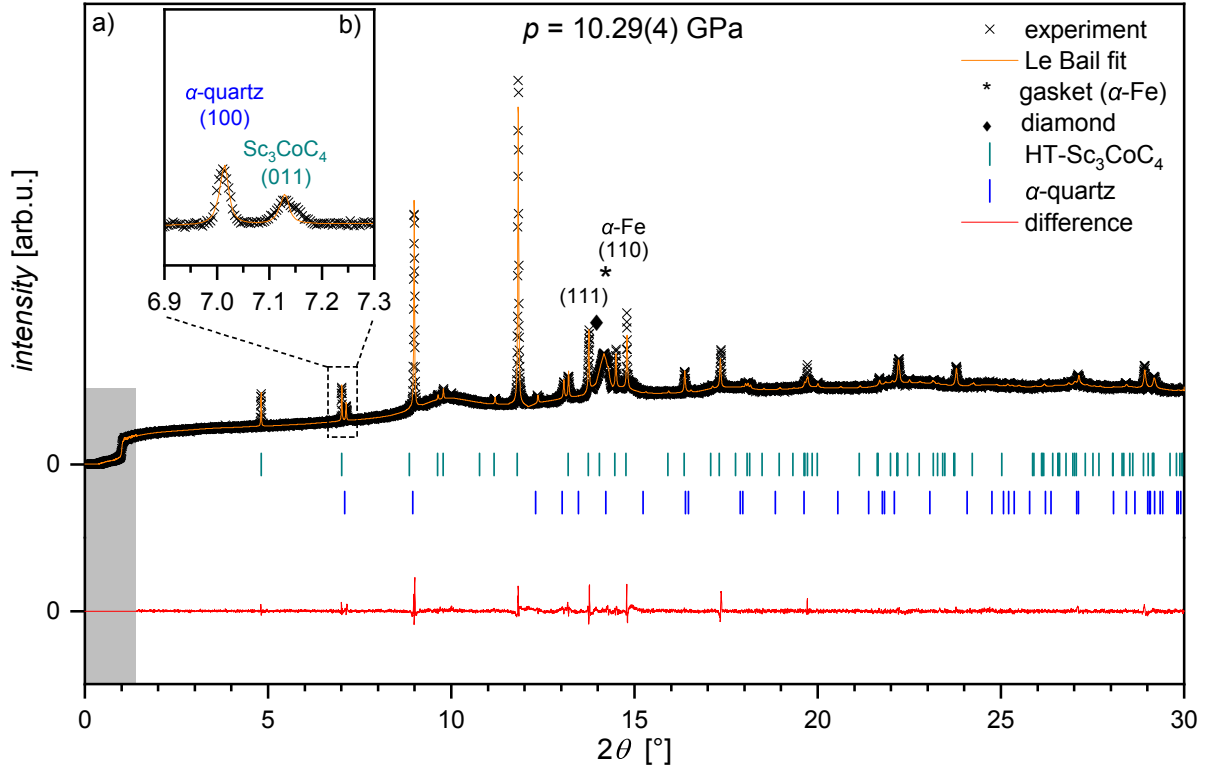


FIG. S11. (a) Room-temperature powder x-ray diffraction pattern (black crosses), Le Bail fit (orange line) and according difference plot (red line) for a Sc_3CoC_4 sample at a pressure of 10.29(4) GPa ($\lambda = 0.49573 \text{ \AA}$). Expected reflection positions for Sc_3CoC_4 in its high-temperature phase and α -quartz are indicated by green and blue bars, respectively. Asterisks and diamonds mark the positions of parasitic reflections from the gasket and the pressure-cell diamonds, while regions excluded from the Le Bail fit are shaded in gray. (b) Enlarged view of the (011) reflection for Sc_3CoC_4 and the (100) reflection for α -quartz.

p [GPa]	GoF	Rp	wRp	a [Å]	b [Å]	c [Å]	V [Å ³]
0	1.21	1.44	1.91	3.39685(15)	4.37375(17)	11.9971(6)	178.240(13)
0.106(1)	1.22	1.56	1.97	3.39617(12)	4.37311(14)	11.9929(4)	178.116(11)
0.255(1)	1.24	1.60	1.99	3.39496(9)	4.37225(11)	11.9899(3)	177.974(8)
0.637(3)	1.12	1.46	1.78	3.39235(10)	4.36986(10)	11.9807(3)	177.603(8)
0.932(6)	1.27	1.56	2.02	3.39015(11)	4.36772(16)	11.9742(4)	177.304(10)
1.674(14)	1.22	1.49	1.94	3.38515(13)	4.36153(16)	11.9589(5)	176.566(12)
2.148(6)	1.23	1.55	1.95	3.38207(13)	4.35809(13)	11.9480(5)	176.106(11)
2.882(4)	1.20	1.51	1.90	3.37662(13)	4.35417(16)	11.9330(5)	175.443(12)
3.562(18)	1.40	1.71	2.22	3.37207(7)	4.34944(18)	11.9181(5)	174.799(11)
4.286(9)	1.20	1.47	1.91	3.36744(18)	4.3451(2)	11.9033(6)	174.167(16)
6.164(5)	1.30	1.63	2.05	3.35590(16)	4.3339(2)	11.8685(6)	172.618(15)
6.734(8)	1.20	1.54	1.89	3.35206(11)	4.33076(15)	11.8586(4)	172.151(10)
7.533(4)	1.31	1.67	2.07	3.34729(12)	4.32606(13)	11.8457(4)	171.533(10)
8.380(12)	1.30	1.57	2.03	3.34208(15)	4.32134(18)	11.8287(5)	170.833(13)
8.59(2)	1.28	1.58	2.00	3.34090(14)	4.31987(16)	11.8243(5)	170.652(12)
8.80(3)	1.25	1.50	1.96	3.33961(14)	4.31831(16)	11.8204(4)	170.467(11)
9.15(4)	1.30	1.59	2.05	3.33732(17)	4.3164(2)	11.8137(6)	170.180(14)
9.53(6)	1.18	1.45	1.86	3.3343(2)	4.3149(3)	11.8053(6)	169.844(19)
9.89(4)	1.27	1.60	1.99	3.3313(3)	4.3132(3)	11.8040(8)	169.61(2)
10.29(4)	1.18	1.50	1.88	3.3275(3)	4.3121(4)	11.7985(11)	169.29(3)

TABLE I. Pressure-dependent variation of the profile Rp factors and refined lattice parameters for the Le Bail fits of all high-pressure powder x-ray diffraction patterns.

VI. SINGLE-CRYSTAL X-RAY DIFFRACTION EXPERIMENTS

A. Data collection and reduction

All single-crystal x-ray diffraction studies were performed using a four-circle Eulerian cradle goniometer (HUBER) and a sample-to-detector distance of 7 cm. Reflection intensities were collected by a Pilatus 300K pixel detector with a CdTe detection layer (DECTRIS). A micro-focus AgK α tube ($\lambda = 0.56087 \text{ \AA}$) with a montel multilayer optic (INCOATEC) served as x-ray source.

Sample cooling to a minimum temperature of 11 K was done with a closed-cycle helium cryocooler (ARS). Two alternative types of heat and radiation shields (outer and optional inner shield) were used: Stainless steel shields equipped with Kapton windows that add only a weak and continuous background to the collected x-ray diffraction images but strongly restrict the accessible portion of reciprocal space, and beryllium shields (domes) that allow the measurement of a larger number of reflection intensities but create stronger parasitic scattering in the form of speckled rings (see Fig. S12b). The type of heat and radiation shields employed in each experiment is specified in Tab. II and Tab. III.

High pressure was generated by commercially available diamond anvil cells (DACs; see Tab. II and Tab. III) of Diacell Tozer-type (ALMAX EASYLAB) and of Boehler-plate-type (ALMAX EASYLAB) equipped with conical Boehler-Almax anvils (culet diameter $600 \mu\text{m}$).²⁵⁻²⁷ Due to its smaller size the first DAC type was mounted inside the sample chamber of the closed-cycle cryostat, whereas the latter DAC type was only operated at room temperature (employed pressure-transmitting media are listed in Tab. II and Tab. III). Specified pressure values were always determined ahead of the x-ray diffraction experiment at room temperature using the fluorescence signal of ruby spheres inside the pressure chamber.²⁸⁻³⁰

In case of ambient-pressure low-temperature studies without pressure cell parasitic scattering from the beryllium heat and radiation shields was determined and subtracted explicitly (procedure illustrated in Fig. S12). For this purpose, the investigated sample was translated reproducibly out of and into the x-ray beam using a linear nanopositioner (AT-TOCUBE). In case of high-pressure studies masks were applied to regions of the diffraction images shadowed by the DAC body or dominated by strong Bragg reflections from the DAC diamonds (Fig. S13). Additionally the two strongest innermost Debye rings of beryllium

were masked (compare Fig. S13a and Fig. S13b) in case of high-pressure low-temperature measurements.

Reflection intensities were evaluated employing the EVAL14 suite of programs^{31,32} and subjected to scaling and absorption correction employing SADABS/TWINABS.³³ Structural models were refined with the program JANA2006²³ using the HKLF4 reflection format for untwinned and the HKLF5 reflection format for systematically twinned samples below the HT→LT phase transition.

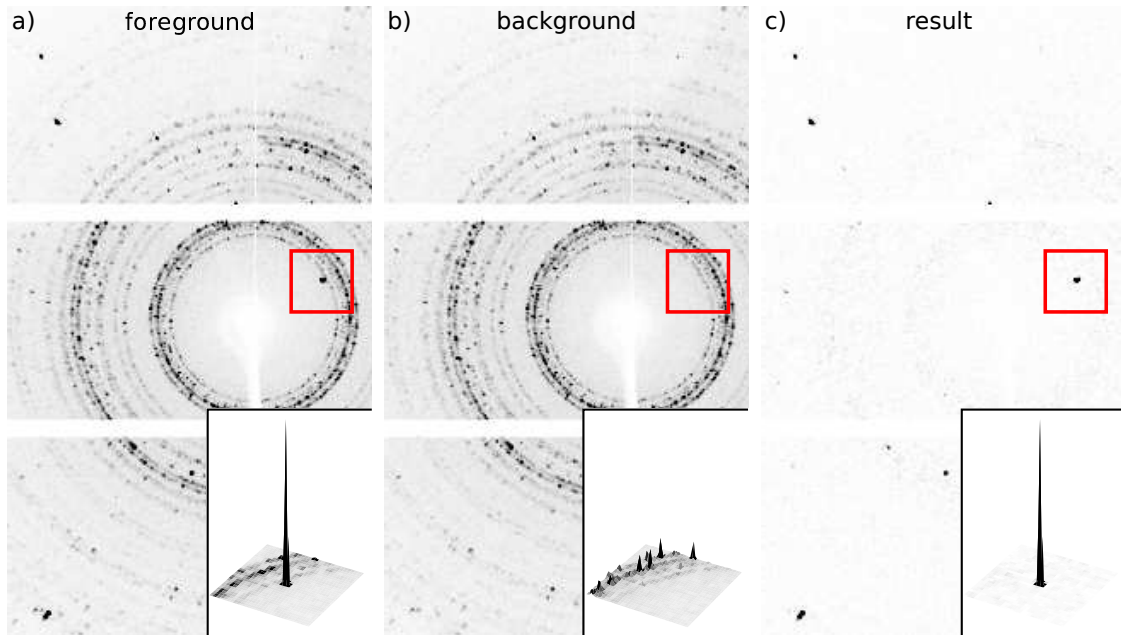


FIG. S12. Background subtraction procedure for ambient-pressure low-temperature measurements without pressure cell: For each x-ray diffraction image (a) an individual background (b) is determined by translating the sample out of the beam. Subtraction of the background leads to the result displayed in (c). Insets show 3D profiles of the regions marked by red rectangles. Note that the inset in (b) is plotted with an eight times enlarged z scale.

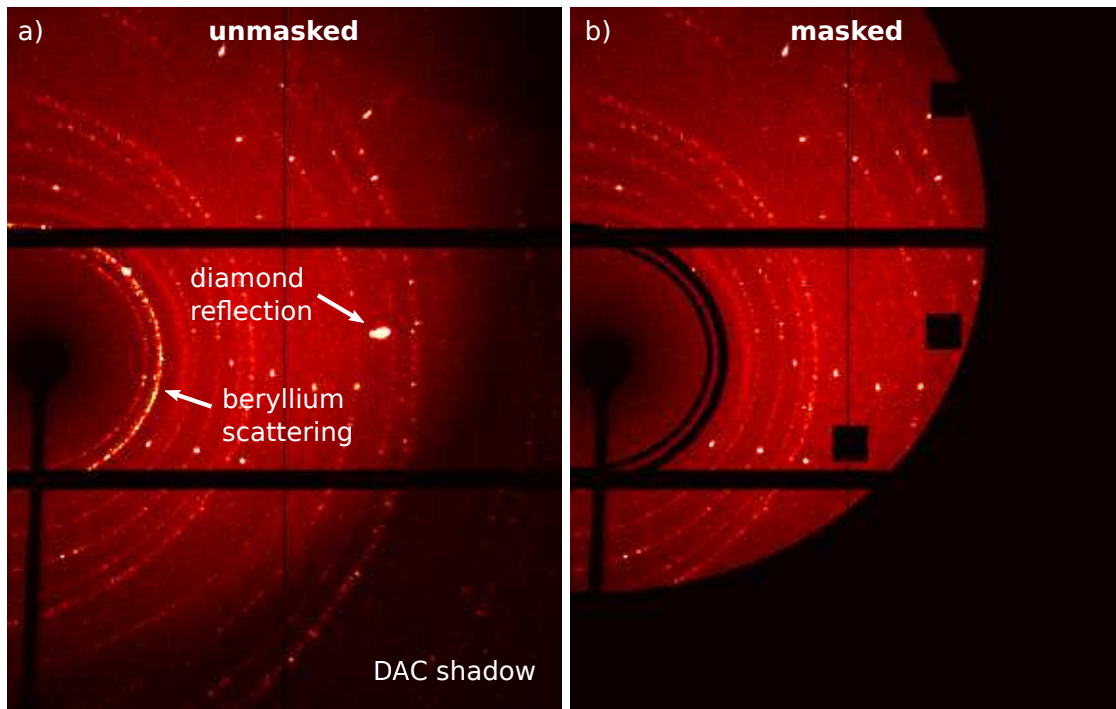


FIG. S13. X-ray diffraction image from a high-pressure low-temperature experiment (a) before and (b) after application of masks to cover regions shadowed by the DAC body, diamond reflections and prominent Debye rings from the beryllium heat and radiation shield.

B. Overview of experiments

	1	2	3
sample dim. [μm^3]	40×51×290	55×131×141	68×116×126
sample photo	Fig. S2	Fig. S3a	Fig. S3b
pressure [GPa]	ambient	ambient / 0.6, 1.9, 4.0, 5.5	ambient / 4
pressure cell ^a	–	Tozer DAC	Tozer DAC
culet diam. [μm]	–	600	600
press. chamber diam. [μm]	–	285	270
press. chamber height. [μm]	–	90	88
press. determ. ^b	–	– / ruby fluoresc.	– / ruby fluoresc.
press. transm. medium	–	– / Daphne 7575	– / Daphne 7575
hydrostat. lim. [GPa] at $T = \text{RT}$	–	– / 3.9 - 4 [34]	– / 3.9 - 4 [34]
temperature [K]	11, 70, 100	22 - 300	36, 106 / 37, 107
sample cryostat	closed cycle He	closed cycle He	closed cycle He
vacuum chamber	beryllium domes	steel cubes	beryllium dome
parasitic scatt./ shadows	subtracted	–	masked

^a sample / ruby spheres were wetted with perfluorinated polyether and placed in the pressure chamber.

^b performed at $T = 294$ K.

TABLE II. Overview of single-crystal x-ray diffraction experiments.

	4	5	6
sample dim. [μm^3]	48×150×152	73×120×186	70×98×98
sample photo	Fig. S3c	Fig. S4a	Fig. S4b
pressure [GPa]	ambient / 4.5	0.2, 4.2	0.1, 5.4, 6.7, 8.1, 10.1
pressure cell ^a	– / Tozer DAC	Boehler DAC	Boehler DAC
culet diam. [μm]	– / 600	600	600
press. chamber diam. [μm]	– / 270	240	255
press. chamber height. [μm]	– / 85	94	92
press. determ. ^b	– / ruby fluoresc.	ruby fluoresc.	ruby fluoresc.
press. transm. medium	– / Daphne 7575	4:1 MeOH:EtOH	4:1 MeOH:EtOH
hydrostat. lim. [GPa] at $T = \text{RT}$	– / 3.9 - 4 [34]	≈ 10 [20]	≈ 10 [20]
temperature [K]	13, RT / 27, RT	RT	RT
sample cryostat	closed cycle He	–	–
vacuum chamber	steel cubes	–	–
parasitic scatt./ shadows	–	masked	masked

^a sample / ruby spheres were wetted with perfluorinated polyether and placed in the pressure chamber.

^b performed at $T = 294$ K.

TABLE III. Overview of single-crystal x-ray diffraction experiments (continued).

C. Ambient-pressure low-temperature measurements without pressure cell

T [K]	11	70	100
unit cell dimensions	$a = 5.53630(10) \text{ \AA}$	$a = 5.53600(10) \text{ \AA}$	$a = 5.53720(10) \text{ \AA}$
	$b = 12.0210(2) \text{ \AA}$	$b = 12.0167(2) \text{ \AA}$	$b = 12.00370(10) \text{ \AA}$
	$c = 5.53640(10) \text{ \AA}$	$c = 5.53590(10) \text{ \AA}$	$c = 5.53710(10) \text{ \AA}$
	$\beta = 104.8070(10)^\circ$	$\beta = 104.7720(10)^\circ$	$\beta = 104.4620(10)^\circ$
	$V = 356.222(11) \text{ \AA}^3$	$V = 356.101(11) \text{ \AA}^3$	$V = 356.372(10) \text{ \AA}^3$
calculated density	$4.5095 \text{ g}\cdot\text{cm}^{-3}$	$4.511 \text{ g}\cdot\text{cm}^{-3}$	$4.5076 \text{ g}\cdot\text{cm}^{-3}$
crystal size		$40 \times 51 \times 290 \text{ \mu m}^3$	
wave length		0.56087 \AA	
transm. ratio (max/min)	$0.747 / 0.686$	$0.747 / 0.633$	$0.747 / 0.646$
absorption coefficient	5.016 mm^{-1}	5.017 mm^{-1}	5.014 mm^{-1}
$F(000)$		456	
θ range	3° to 36°	3° to 37°	3° to 37°
range in hkl		$\pm 11, \pm 25, \pm 11$	
total no. reflections	8720	8390	8509
independent reflections	2142 ($R_{\text{int}} = 0.0123$)	2112 ($R_{\text{int}} = 0.0158$)	2153 ($R_{\text{int}} = 0.0148$)
reflections with $I \geq 2\sigma(I)$	2007	1986	1947
data / parameters	2142 / 43	2112 / 43	2153 / 43
goodness-of-fit on F^2	1.27	1.79	1.44
final R indices [$I \geq 2\sigma(I)$]	$R = 0.0220$	$R = 0.0381$	$R = 0.0302$
	$wR = 0.0414$	$wR = 0.0665$	$wR = 0.0535$
R indices (all data)	$R = 0.0271$	$R = 0.0446$	$R = 0.0389$
	$wR = 0.0424$	$wR = 0.0673$	$wR = 0.0549$
extinction coefficient	$0.0461(14)$	$0.043(2)$	$0.0231(15)$
largest diff. peak and hole	$1.97 / -2.18 \text{ e}\cdot\text{\AA}^{-3}$	$0.65 / -0.86 \text{ e}\cdot\text{\AA}^{-3}$	$1.94 / -2.20 \text{ e}\cdot\text{\AA}^{-3}$

TABLE IV. Crystal data and structure refinements for ambient-pressure single-crystal x-ray diffraction experiments without pressure cell and at temperatures of 11 K, 70 K and 100 K.

	T	fractional atomic coordinates			U_{eq}
atom	[K]	x	y	z	[Å ²]
Co	11	0.26595(2)	0	0.26673(2)	0.00204(3)
	70	0.26559(3)	0	0.26635(3)	0.00240(5)
	100	0.25987(2)	0	0.26046(2)	0.00243(5)
Sc1	11	0.75582(3)	0	0.24273(3)	0.00207(6)
	70	0.75570(4)	0	0.24290(4)	0.00241(9)
	100	0.75383(3)	0	0.24498(3)	0.00239(10)
Sc2	11	0	0.187417(10)	0	0.00210(9)
	70	0	0.187442(16)	0	0.00244(11)
	100	0	0.187747(13)	0	0.00233(10)
Sc3	11	0	0.311540(10)	0.5	0.00210(9)
	70	0	0.311550(16)	0.5	0.00244(11)
	100	0	0.311642(13)	0.5	0.00235(10)
C1	11	0.4110(3)	0.12557(5)	0.0766(2)	0.0031(2)
	70	0.4103(4)	0.12568(7)	0.0763(4)	0.0035(3)
	100	0.4109(3)	0.12514(5)	0.0773(3)	0.0033(3)
C2	11	0.0889(3)	0.12487(5)	0.4233(2)	0.0030(2)
	70	0.0896(4)	0.12490(7)	0.4238(4)	0.0034(3)
	100	0.0890(3)	0.12471(5)	0.4228(3)	0.0033(3)

TABLE V. Refined fractional atomic coordinates and mean-square atomic displacement parameters obtained from ambient-pressure single-crystal x-ray diffraction experiments without pressure cell and at temperatures of 11 K, 70 K and 100 K.

T		mean-square atomic displacement parameters [\AA^2]					
atom	[K]	U_{11}	U_{22}	U_{33}	U_{12}	U_{13}	U_{23}
Co	11	0.00229(6)	0.00176(4)	0.00219(6)	*	0.00082(3)	*
	70	0.00239(9)	0.00275(7)	0.00238(9)	*	0.00120(6)	*
	100	0.00295(10)	0.00192(5)	0.00276(10)	*	0.00136(4)	*
Sc1	11	0.00223(12)	0.00202(5)	0.00195(12)	*	0.00053(5)	*
	70	0.00228(17)	0.00291(9)	0.00216(16)	*	0.00079(9)	*
	100	0.00280(19)	0.00224(6)	0.00220(19)	*	0.00078(5)	*
Sc2	11	0.00295(18)	0.00198(5)	0.00144(17)	*	0.00068(4)	*
	70	0.0036(2)	0.00283(9)	0.00114(19)	*	0.00100(9)	*
	100	0.0034(2)	0.00221(7)	0.00152(19)	*	0.00090(5)	*
Sc3	11	0.00295(18)	0.00196(5)	0.00147(17)	*	0.00071(4)	*
	70	0.0035(2)	0.00281(9)	0.00119(19)	*	0.00094(9)	*
	100	0.0035(2)	0.00218(7)	0.00153(19)	*	0.00087(5)	*
C1	11	0.0017(4)	0.00353(17)	0.0037(4)	0.0005(3)	0.00026(16)	0.0002(3)
	70	0.0015(5)	0.0049(3)	0.0041(6)	0.0002(6)	0.0010(3)	0.0001(6)
	100	0.0027(5)	0.0035(2)	0.0035(5)	0.0002(4)	0.0008(2)	-0.0001(4)
C2	11	0.0019(4)	0.00337(17)	0.0037(4)	-0.0002(3)	0.00039(16)	0.0000(3)
	70	0.0015(5)	0.0050(3)	0.0038(6)	-0.0001(6)	0.0005(3)	0.0002(6)
	100	0.0025(5)	0.0036(2)	0.0036(5)	0.0000(4)	0.0004(2)	0.0003(4)

TABLE VI. Refined mean-square atomic displacement parameters obtained from ambient-pressure single-crystal x-ray diffraction experiments without pressure cell and at temperatures of 11 K, 70 K and 100 K. Parameters marked by an asterisk are forbidden by symmetry.

D. High-pressure low-temperature measurements

T [K]	37	107
	$a = 5.5046(3) \text{ \AA}$	$a = 5.5082(2) \text{ \AA}$
	$b = 11.9698(5) \text{ \AA}$	$b = 11.9729(6) \text{ \AA}$
unit cell dimensions	$c = 5.4723(7) \text{ \AA}$	$c = 5.4832(8) \text{ \AA}$
	$\beta = 105.038(3)^\circ$	$\beta = 104.949(4)^\circ$
	$V = 348.22(5) \text{ \AA}^3$	$V = 349.37(6) \text{ \AA}^3$
calculated density	$4.6131 \text{ g}\cdot\text{cm}^{-3}$	$4.5979 \text{ g}\cdot\text{cm}^{-3}$
crystal size	$68 \times 116 \times 126 \text{ }\mu\text{m}^3$	
wave length	0.56087 \AA	
transm. ratio (max/min)	0.746 / 0.687	0.746 / 0.670
absorption coefficient	5.131 mm^{-1}	5.114 mm^{-1}
$F(000)$	456	
θ range	3° to 33°	
range in hkl	-6/9, -13/19, -5/4	-6/9, -13/20, -5/4
total no. reflections	716	713
independent reflections	212 ($R_{\text{int}} = 0.0048$)	209 ($R_{\text{int}} = 0.0077$)
reflections with $I \geq 2\sigma(I)$	190	178
data / parameters	190 / 18	178 / 18
goodness-of-fit on F^2	3.66	3.81
final R indices [$I \geq 2\sigma(I)$]	$R = 0.0425$	$R = 0.0436$
	$wR = 0.1002$	$wR = 0.1053$
R indices (all data)	$R = 0.0425$	$R = 0.0436$
	$wR = 0.1002$	$wR = 0.1053$
extinction coefficient	–	–
largest diff. peak and hole	$0.69 / -0.76 \text{ e}\cdot\text{\AA}^{-3}$	$0.90 / -1.17 \text{ e}\cdot\text{\AA}^{-3}$

TABLE VII. Crystal data and structure refinements for single-crystal x-ray diffraction experiments at a pressure of 4 GPa and temperatures of 37 K and 107 K.

	T	fractional atomic coordinates			U_{eq}
atom	[K]	x	y	z	[Å ²]
Co	37	0.26648(19)	0	0.2672(3)	0.0027(3)
	107	0.2663(2)	0	0.2666(3)	0.0035(4)
Sc1	37	0.7565(2)	0	0.2417(3)	0.0025(4)
	107	0.7564(3)	0	0.2418(4)	0.0033(4)
Sc2	37	0	0.18764(9)	0	0.0025(4)
	107	0	0.18771(10)	0	0.0032(4)
Sc3	37	0	0.31118(9)	0.5	0.0028(4)
	107	0	0.31122(10)	0.5	0.0037(4)
C1	37	0.4147(12)	0.1261(3)	0.0837(17)	0.0042(8)
	107	0.4137(14)	0.1262(4)	0.0840(19)	0.0057(9)
C2	37	0.0854(13)	0.1250(3)	0.4160(17)	0.0042(8)
	107	0.0867(14)	0.1248(4)	0.4169(19)	0.0057(9)

TABLE VIII. Refined fractional atomic coordinates and mean-square atomic displacement parameters obtained from single-crystal x-ray diffraction experiments at a pressure of 4 GPa and temperatures of 37 K and 107 K.

E. Superstructure reflections at room temperature

Superstructure reflections indicative of the low-temperature phase of Sc_3CoC_4 could be preserved up to room temperature at a pressure of 5.5 GPa, *i.e.* above the hydrostatic limit of the employed pressure medium Daphne 7575³⁴ (experiment 2 in Tab. II; see reconstruction of the $(h0.5l)$ reciprocal-space plane in Fig. S14b). But this was only possible after cooling the sample to 22 K and heating it back to room temperature and at the cost of a deterioration of the sample crystallinity (see broadened reflections in the reconstructed $(h0l)$ plane in Fig. S14a).

We did not succeed in inducing the phase transition between high-temperature and low-temperature phase by pressure application at room temperature alone (experiment 6 in Tab. III). As can be recognized from the reconstructed $(h0.5l)$ planes in Fig. S15 and the x-ray diffraction images in Fig. S16, no superstructure reflections could be observed in a room-temperature high-pressure experiment up to a maximum pressure of 10.1 GPa.

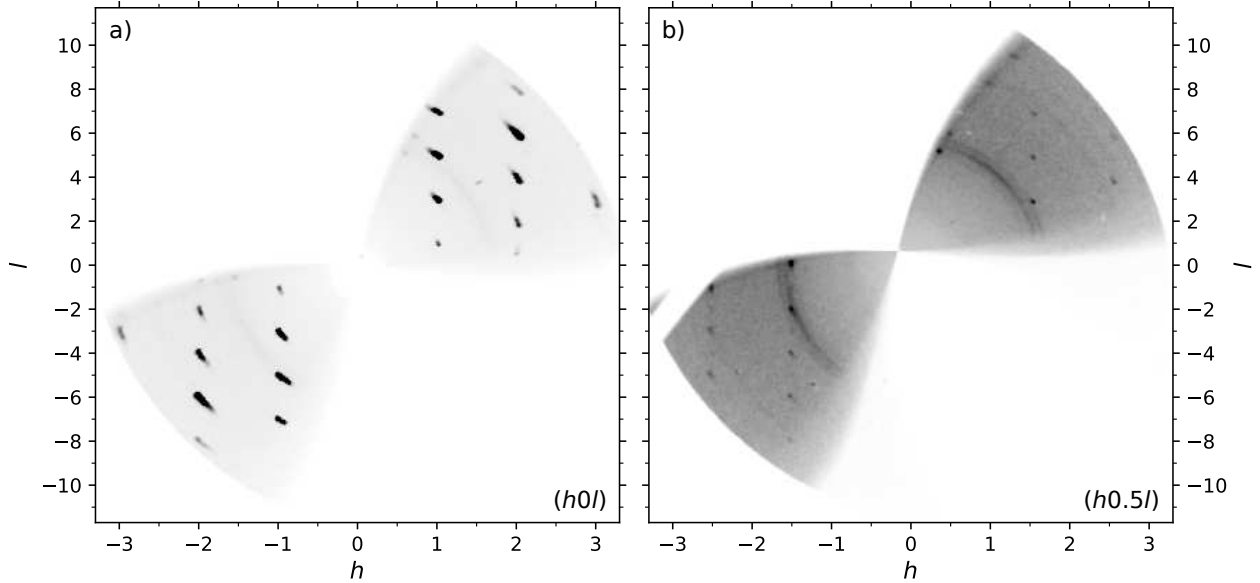


FIG. S14. Reconstructions of reciprocal-space planes (a) $(h0l)$ and (b) $(h0.5l)$ from room-temperature x-ray diffraction data collected after applying a pressure of 5.5 GPa, cooling to 22 K and heating to room temperature again.

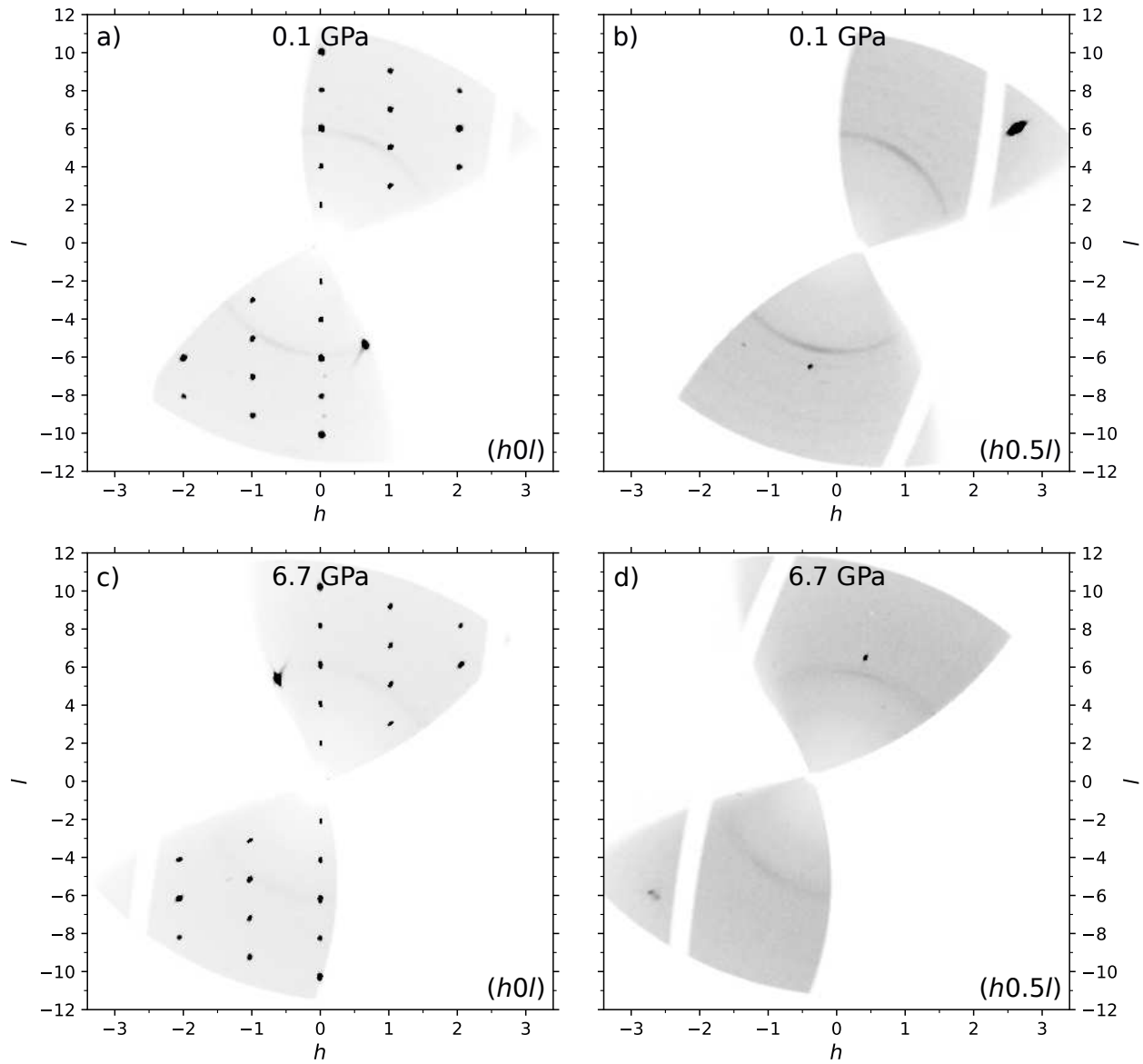


FIG. S15. Reconstructions of reciprocal-space planes $(h0l)$ and $(h0.5l)$ from x-ray diffraction data collected at room-temperature and at pressures of 0.1 GPa (a, b) and 6.7 GPa (c, d). Parasitic scattering from gasket and diamonds leads to ring-shaped features and broad intense reflections, respectively.

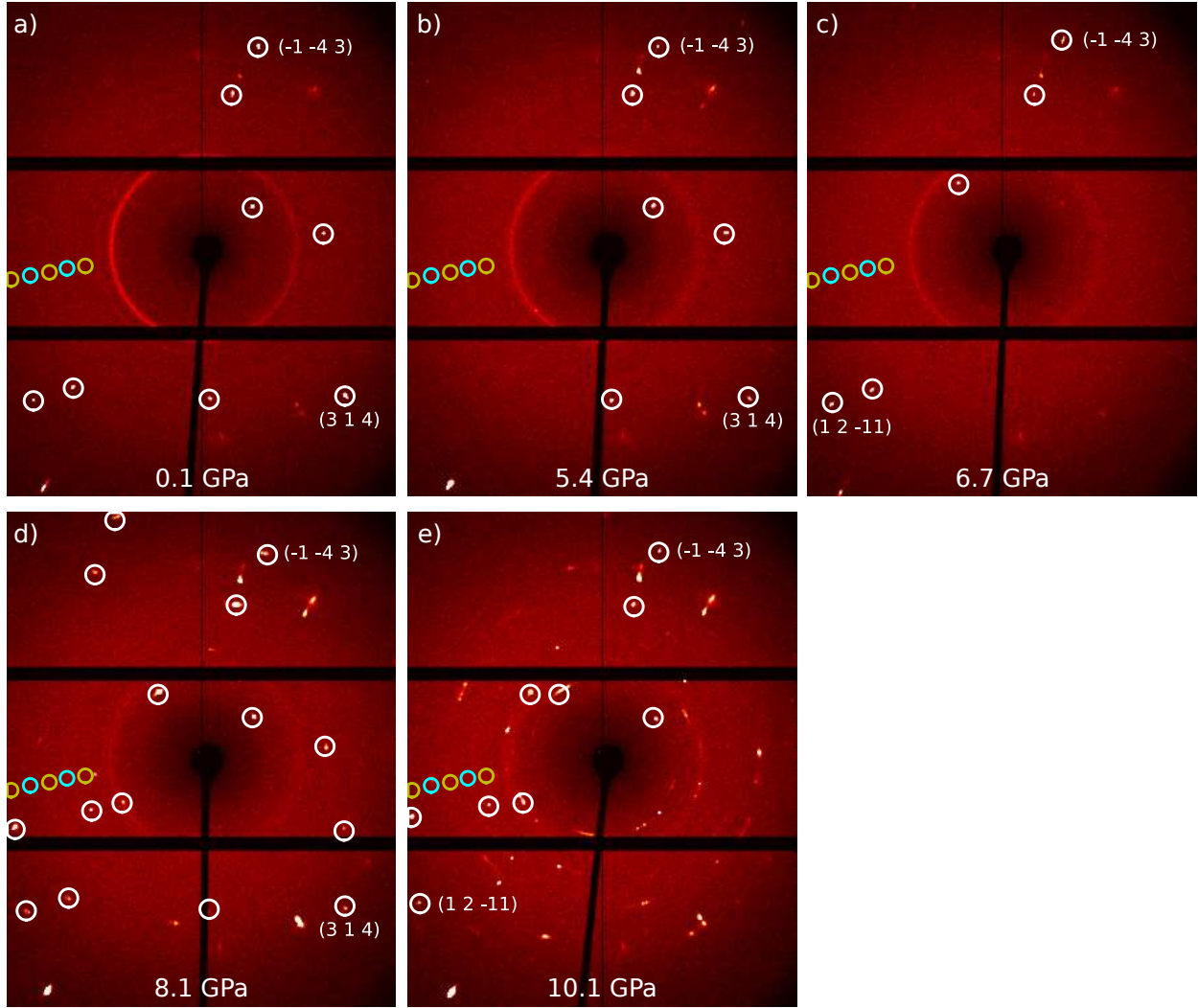


FIG. S16. Selected x-ray diffraction images collected at room temperature and up to a maximum pressure of 10.1 GPa with nearly unchanged orientation of the pressure cell. Main reflections expected for the high-temperature phase of Sc_3CoC_4 are indicated by white circles. The positions of superstructure reflections indicative of a transition into the low-temperature phase are marked by yellow (twin domain 1) and cyan circles (twin domain 2).

F. Test for sample degradation in high-pressure/low-temperature studies

To exclude irreversible changes or a degradation of the sample quality in our combined high-pressure/low-temperature studies we reenacted a typical experimental procedure and collected x-ray diffraction data after each step (experiment 4 in Tab. III). Reconstructions of reciprocal-space planes ($h0l$) and ($h0.5l$) obtained for a Sc_3CoC_4 single crystal at ambient conditions (see Fig. S17a and Fig. S17b) and at 13 K (Fig. S17c and Fig. S17d) demonstrate the quality of the investigated sample. Notably, a column of superstructure reflections along the c^* axis with equal contributions from two distinct twin domains can be recognized in Fig. S17d.

Inserting the single crystal into the pressure chamber of a Tozer-type diamond anvil cell (DAC) and applying a pressure of 4.5 GPa leaves the sample crystallinity unchanged (Fig. S17e and Fig. S17f; ring-shaped features and additional reflections are due to parasitic x-ray scattering from the gasket and the DAC diamonds, respectively). This does not change by cooling the pressure cell to 27 K (Fig. S18a and Fig. S18b). As pointed out in the main paper, every second reflection in the columns of superstructure reflections along c^* in Fig. S18b is now absent due to a pressure-induced detwinning process.

Still, all pressure-induced changes to the sample are fully reversible. This is pointed out by sharp profiles of the Bragg reflections in the ($h0l$) plane (Fig. S18c) and the absence of scattered intensity in the ($h0.5l$) plane (Fig. S18d) after heating to room temperature and removing the single crystal from the pressure chamber of the DAC. Furthermore, the effect of cooling to 13 K again without applied pressure is consistent with the measurements before the high-pressure study (compare Fig. S18e and Fig. S18f with Fig. S17c and Fig. S17d). Namely, reflections in the ($h0l$) plane are preserved and complete columns of superstructure reflections along c^* featuring contributions from two twin domains appear.

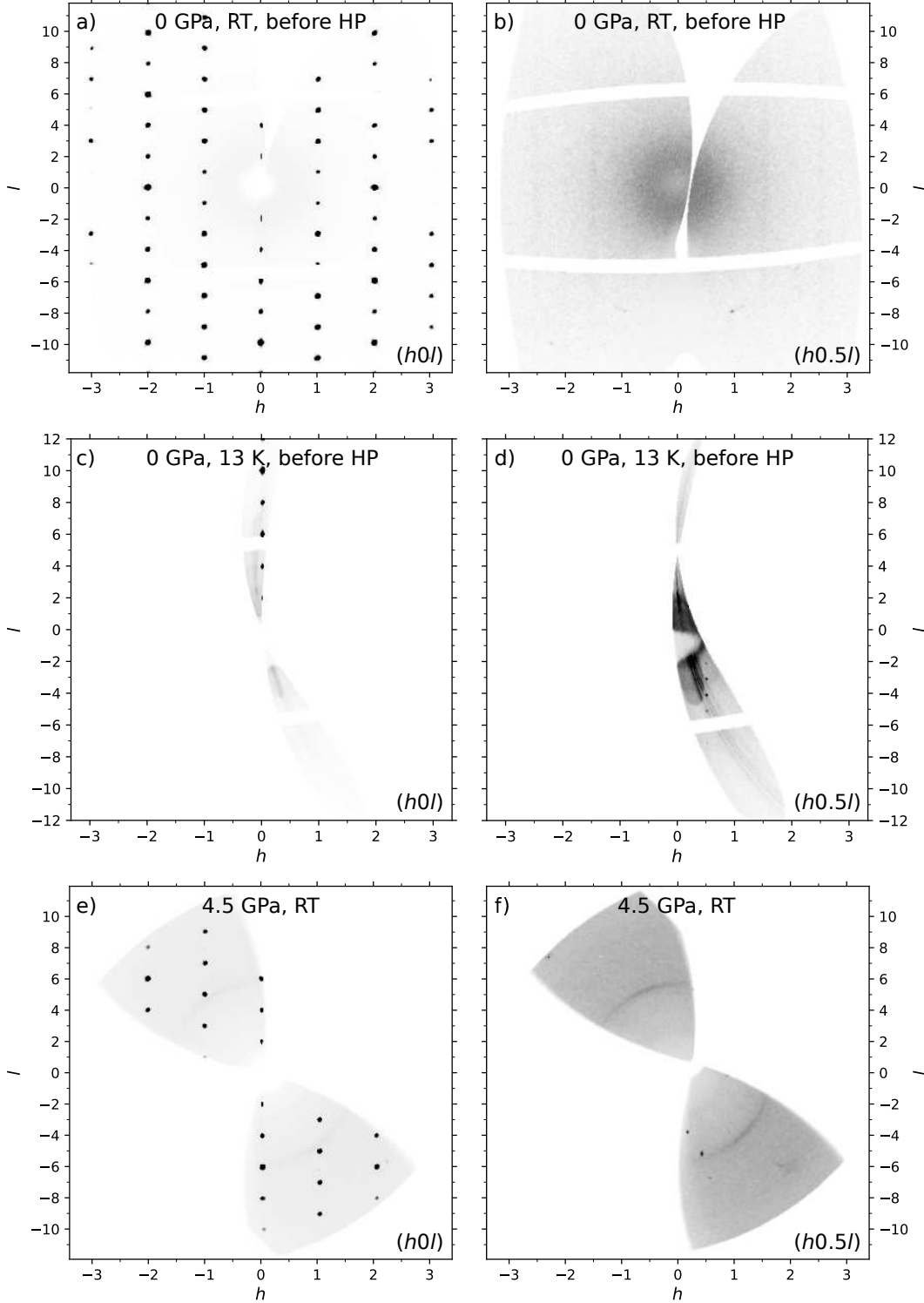


FIG. S17. Reconstructions of reciprocal-space planes $(h0l)$ and $(h0.5l)$ from x-ray diffraction data collected under various conditions, *i.e.* at room-temperature (a, b) and 13 K (c, d) before performing a high-pressure (HP) experiment, and again at room-temperature but with an applied pressure of 4.5 GPa (e, f).

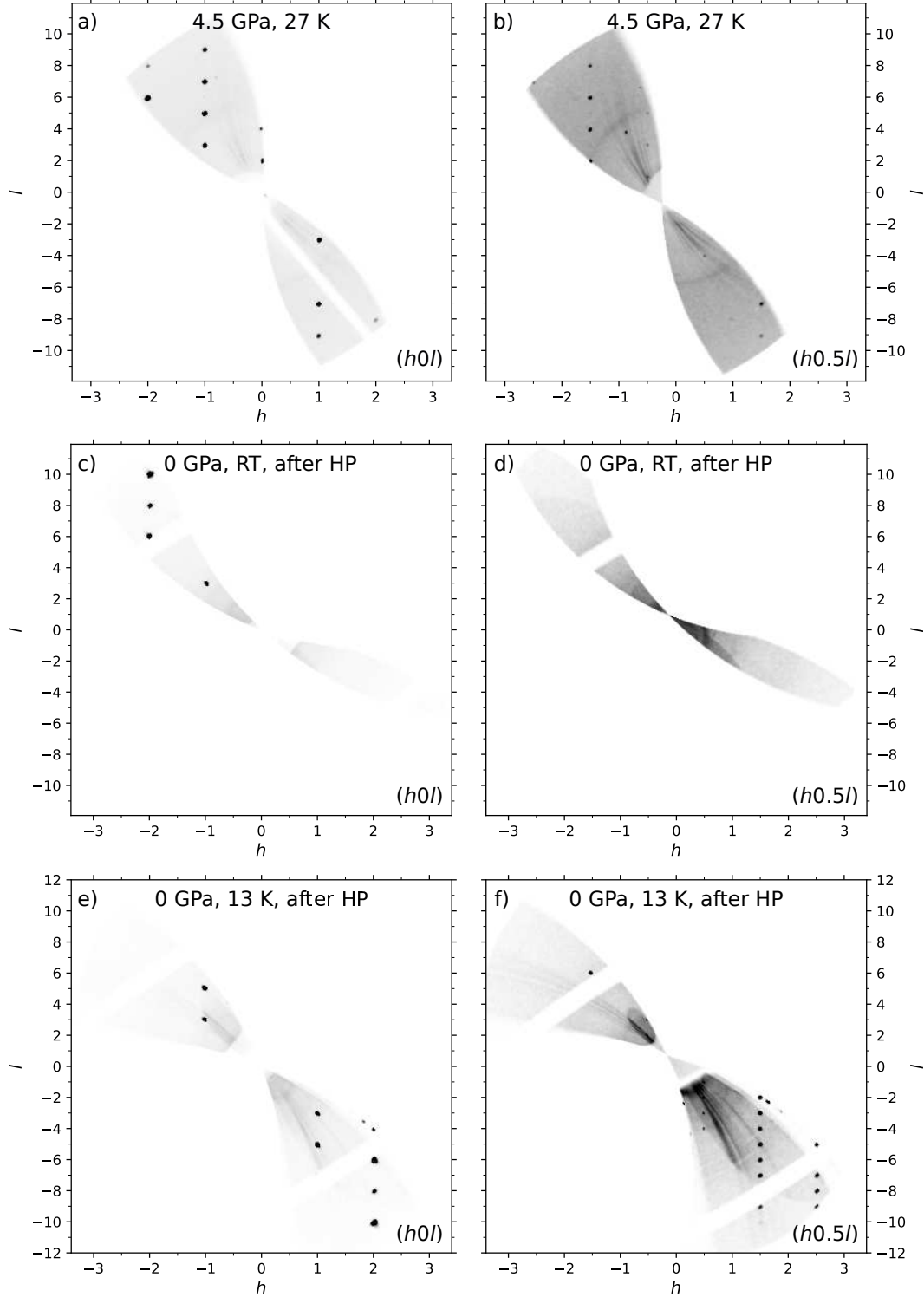


FIG. S18. Reconstructions of reciprocal-space planes $(h0l)$ and $(h0.5l)$ from x-ray diffraction data collected under various conditions, *i.e.* at 27 K with an applied pressure of 4.5 GPa (a, b), at room temperature after removing the crystal from the high-pressure (HP) cell (c, d) and after cooling to 13 K again (e, f).

G. High-pressure measurements at room temperature

As pointed out in Sec. VIE, we did not succeed in forcing the transition between the high-temperature and low-temperature phase of Sc_3CoC_4 in high-pressure experiments at room temperature. Still, the HT phase structure provides some flexibility to react to applied pressure, *e.g.* the position of the carbon atoms. Therefore, we investigated the effect of pressure on the HT phase structure by performing x-ray diffraction experiments at 0.2 GPa and 4.2 GPa (experiment 5 in Tab. III, crystal and refinement details are available in Tab. IX, fractional coordinates and mean-square atomic displacement parameters in Tab. X and Tab. XI).

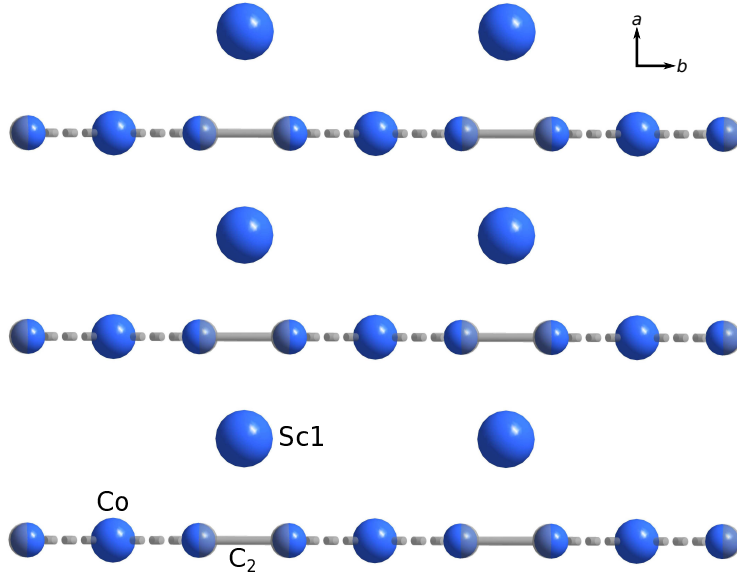


FIG. S19. Overlay of the refined atomic positions within a layered building unit of Sc_3CoC_4 at room temperature and applied pressures of 0.2 GPa (gray, semi-transparent) and 4.2 GPa (blue, non-transparent). All atom displacements are exaggerated seven-fold, Sc2 and Sc3 atoms have been omitted for clarity. The given coordinate system refers to the orthorhombic unit cell of the high-temperature phase.

Upon pressure application the distance between adjacent $[\text{Co}(\text{C}_2)_2]_\infty$ ribbons along the a axis is reduced from $3.3998(9)$ Å to $3.3701(9)$ Å (all values are given with their threefold standard deviation). Analogously, a compression from $6.0061(8)$ Å to $5.9670(5)$ Å is found for the distance between adjacent quasi-2D Sc1-Co-C layers. Inspection of the overlaid atomic positions at 0.2 GPa and 4.2 GPa in Fig. S19 reveals no major pressure-induced changes.

Only the C–C bond distance expands insignificantly from 1.452(9) Å to 1.455(9) Å, while the Co–C bond distance is compressed from 2.094(4) Å to 2.078(3) Å.

p [GPa]	0.2	4.2
unit cell dimensions	$a = 3.3998(3)$ Å	$a = 3.3701(3)$ Å
	$b = 4.3738(2)$ Å	$b = 4.35220(10)$ Å
	$c = 12.0121(5)$ Å	$c = 11.9340(3)$ Å
	$V = 178.620(19)$ Å ³	$V = 175.040(17)$ Å ³
calculated density	4.4966 g·cm ⁻³	4.5886 g·cm ⁻³
crystal size	73×120×186 μm ³	
wave length	0.56087 Å	
transm. ratio (max/min)	0.747 / 0.677	0.747 / 0.659
absorption coefficient	5.001 mm ⁻¹	5.104 mm ⁻¹
$F(000)$	228	
θ range	3° to 35°	
range in hkl	-2/2, -8/5, -14/24	
total no. reflections	880	871
independent reflections	178 ($R_{\text{int}} = 0.0086$)	172 ($R_{\text{int}} = 0.0087$)
reflections with $I \geq 2\sigma(I)$	169	165
data / parameters	178 / 14	172 / 14
goodness-of-fit on F^2	1.99	2.03
final R indices [$I \geq 2\sigma(I)$]	$R = 0.0172$	$R = 0.0159$
	$wR = 0.0473$	$wR = 0.0475$
R indices (all data)	$R = 0.0180$	$R = 0.0165$
	$wR = 0.0474$	$wR = 0.0476$
extinction coefficient	–	
largest diff. peak and hole	0.55 / -0.60 e·Å ⁻³	0.39 / -0.46 e·Å ⁻³

TABLE IX. Crystal data and structure refinements for single-crystal x-ray diffraction experiments at room temperature and at pressures of 0.2 GPa and 4.2 GPa.

	p	fractional atomic coordinates			$U_{\text{iso}}/U_{\text{eq}}$
atom	[GPa]	x	y	z	[\AA^2]
Co	0.2	0	0.5	0	0.0039(3)
	4.2	0	0.5	0	0.0035(3)
Sc1	0.2	0.5	0	0	0.0035(4)
	4.2	0.5	0	0	0.0038(4)
Sc2	0.2	0.5	0.5	0.18808(3)	0.0034(3)
	4.2	0.5	0.5	0.18827(2)	0.0032(4)
C1	0.2	0.5	0.6660(3)	0.37515(10)	0.0047(2)
	4.2	0.5	0.6671(3)	0.37516(9)	0.0039(2)

TABLE X. Refined fractional atomic coordinates and mean-square atomic displacement parameters obtained from single-crystal x-ray diffraction experiments at room temperature and at pressures of 0.2 GPa and 4.2 GPa. Note that the carbon atom was refined isotropically.

	p	mean-square atomic displacement parameters [\AA^2]					
atom	[GPa]	U_{11}	U_{22}	U_{33}	U_{12}	U_{13}	U_{23}
Co	0.2	0.0051(10)	0.00355(18)	0.00301(13)	*	*	*
	4.2	0.0042(9)	0.00328(18)	0.00294(12)	*	*	*
Sc1	0.2	0.0029(12)	0.0040(2)	0.00372(16)	*	*	*
	4.2	0.0036(13)	0.0037(2)	0.00390(16)	*	*	*
Sc2	0.2	0.0031(10)	0.00355(18)	0.00348(12)	*	*	*
	4.2	0.0031(10)	0.00316(18)	0.00337(13)	*	*	*

TABLE XI. Refined mean-square atomic displacement parameters obtained from single-crystal x-ray diffraction experiments at room temperature and at pressures of 0.2 GPa and 4.2 GPa. Parameters marked by an asterisk are forbidden by symmetry. The carbon atom was refined isotropically.

VII. PHONON DISPERSION RELATIONS UNDER UNIAXIAL STRAIN

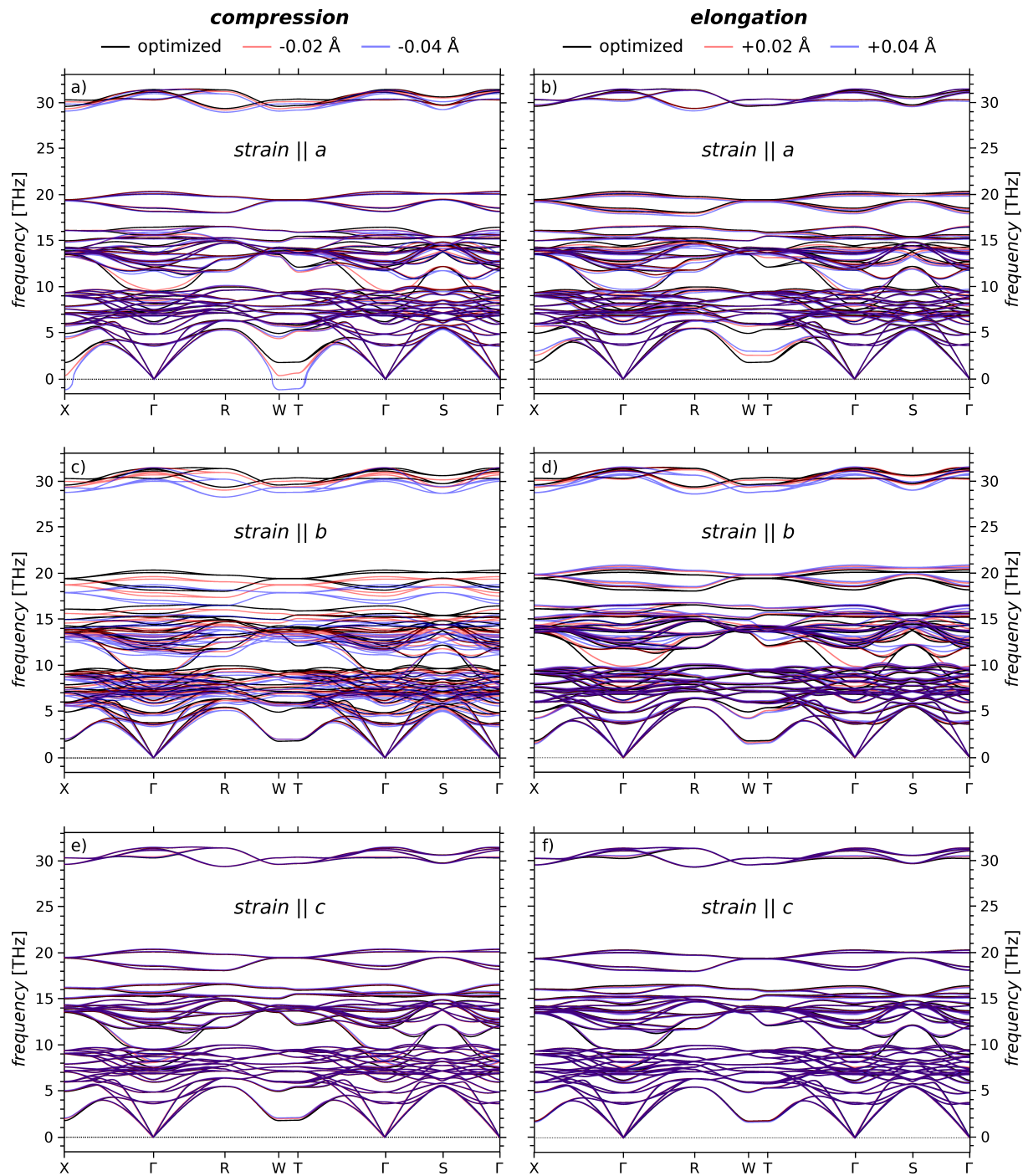


FIG. S20. Response of the phonon dispersion of HT Sc_3CoC_4 (DFT study) to a compression or elongation of the lattice parameters a (a, b), b (c, d) and c (e, f).

VIII. ANALYSIS OF EXPERIMENTAL DATA

A. Calculation of atom displacements

Displacements Δr_{Co} of the cobalt atoms from their positions in the high-temperature phase of Sc_3CoC_4 were calculated from the difference between the longer Co–Co distance d_2 and the shorter Co–Co distance d_1 (see Fig. S21a):

$$\Delta r_{\text{Co}} = \frac{1}{4}(d_2 - d_1) . \quad (1)$$

An analogous procedure was applied for the calculation of the scandium atom (Sc1) displacements Δr_{Sc1} (see Fig. S21b):

$$\Delta r_{\text{Sc1}} = \frac{1}{4}(d'_2 - d'_1) . \quad (2)$$

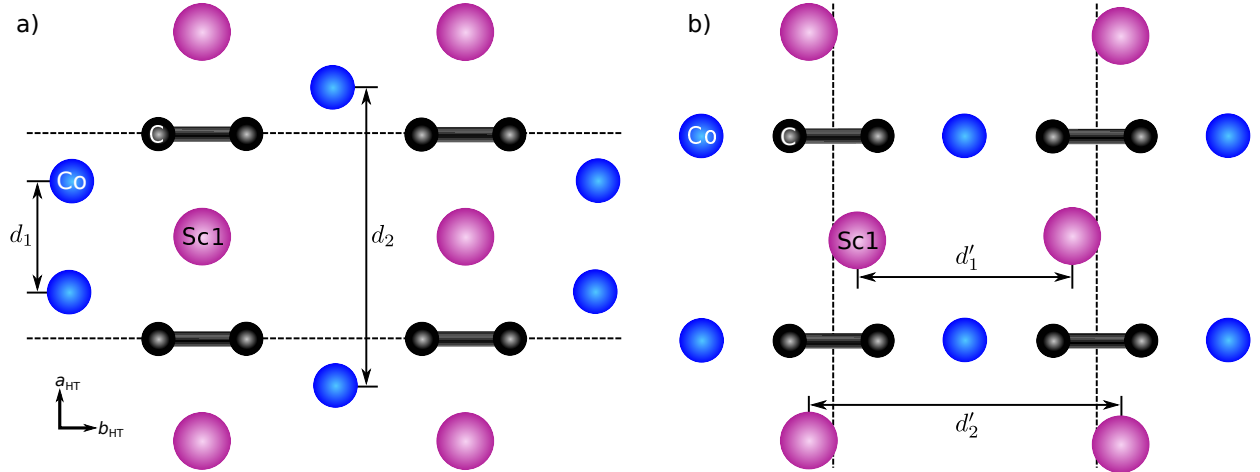


FIG. S21. Location of short and long distances between (a) cobalt and (b) scandium (Sc1) atoms in the low-temperature (LT) phase structure of Sc_3CoC_4 . For clarity, only the displacements of the Co (a) or Sc1 atoms (b) from their high-temperature (HT) phase positions are depicted. The given coordinate system refers to the orthorhombic unit cell of the HT phase.

The rotation angle $\Delta\alpha_{\text{C}}$ of the C_2 units is spanned by the vector

$$\vec{v} = A^T(X_{\text{C}_b} - X_{\text{C}_a}) \quad (3)$$

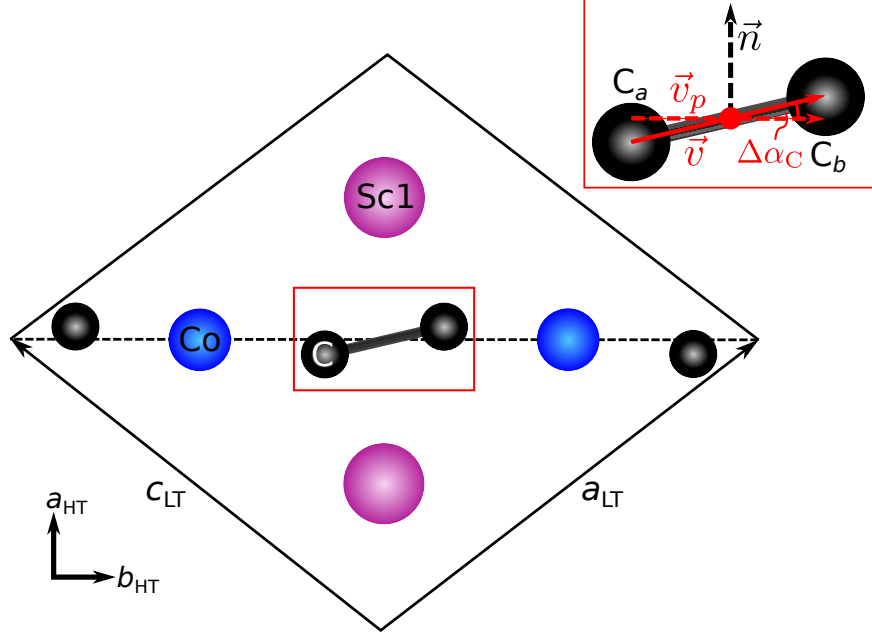


FIG. S22. Projection of the low-temperature (LT) phase unit cell of Sc_3CoC_4 into the $a_{\text{LT}}/c_{\text{LT}}$ plane (coordinate system corresponding to the unit cell of the orthorhombic high-temperature (HT) phase in the lower left corner). For clarity, only the displacements of the carbon atoms from their HT phase positions are depicted. The location of vectors \vec{v} , \vec{v}_p and \vec{n} required for the calculation of the C_2 unit rotation angle $\Delta\alpha_{\text{C}}$ (see text) is indicated in the inset.

connecting the two constituent carbon atoms C_a and C_b (red solid arrow in Fig. S22) and its projection

$$\vec{v}_p = \vec{v} - (\vec{v} \cdot \vec{n}) \vec{n} \quad (4)$$

into the plane of undisplaced carbon atoms (red dashed arrow in Fig. S22). X_{C_a} and X_{C_b} denote fractional coordinate matrices, while A denotes the basis vector matrix of the low-temperature phase unit cell

$$A^T = \left(\vec{a}_{\text{LT}} \ \vec{b}_{\text{LT}} \ \vec{c}_{\text{LT}} \right). \quad (5)$$

Furthermore, the normal vector \vec{n} of the plane of undisplaced carbon atoms (black dashed arrow in Fig. S22) is calculated from the basis vectors of the low-temperature phase unit cell as

$$\vec{n} = \frac{(\vec{a}_{\text{LT}} - \vec{c}_{\text{LT}}) \times \vec{b}_{\text{LT}}}{|(\vec{a}_{\text{LT}} - \vec{c}_{\text{LT}}) \times \vec{b}_{\text{LT}}|}. \quad (6)$$

In a final step, the value of $\Delta\alpha_{\text{C}}$ can be obtained using the inner product of \vec{v} and \vec{v}_p

$$\Delta\alpha_{\text{C}} = \arccos\left(\frac{\vec{v} \cdot \vec{v}_p}{|\vec{v}||\vec{v}_p|}\right). \quad (7)$$

B. Sensitivity of superstructure reflection intensities to atom displacements

Information about the displacements of Co, Sc1 and C atoms from their positions in the high-temperature (HT) phase of Sc_3CoC_4 is encoded in the intensities of main and superstructure reflections. To further elucidate the nature and size of these changes we repeatedly calculated reflection intensities for rigid structural models with different positions of Co, Sc1 and C atoms using the software JANA2006.²³

As a starting point the Co, Sc1 and C atoms in a structural model of the ambient-pressure low-temperature (LT) phase at 11 K (see Tab. IV, Tab. V and Tab. VI) were reset to their high-symmetry positions in the HT phase (see Tab. XII). Furthermore, anisotropic atomic displacement parameters (ADPs) were replaced by isotropic ones (Tab. XII) and the twin ratio was fixed to a value of 0.5. The atoms were then displaced individually and stepwise into the direction of their LT phase positions, *i.e.* the Co and Sc1 atoms were moved linearly and the C_2 units were rotated in a conrotatory or disrotatory fashion. At each step, only reflection intensities were calculated without refining the model parameters. Ensuing changes in the averaged intensity of main and superstructure reflections are displayed in Fig. S23a and Fig. S23b, while Fig. S23c and Fig. S23d show changes in the intensity of a specific strongly reacting main and superstructure reflection.

atom	fractional atomic coordinates			U_{iso}
	x	y	z	$[\text{\AA}^2]$
Co	0.25	0	0.25	0.002035
Sc1	0.75	0	0.25	0.002068
Sc2	0	0.18801	0	0.002103
Sc3	0	0.31199	0.5	0.002100
C1	0.41693	0.12557	0.08307	0.003063
C2	0.08307	0.12487	0.41693	0.003034

TABLE XII. Fractional atomic coordinates and mean-square atomic displacement parameters used in the initial structural model for the calculation of reflection intensities.

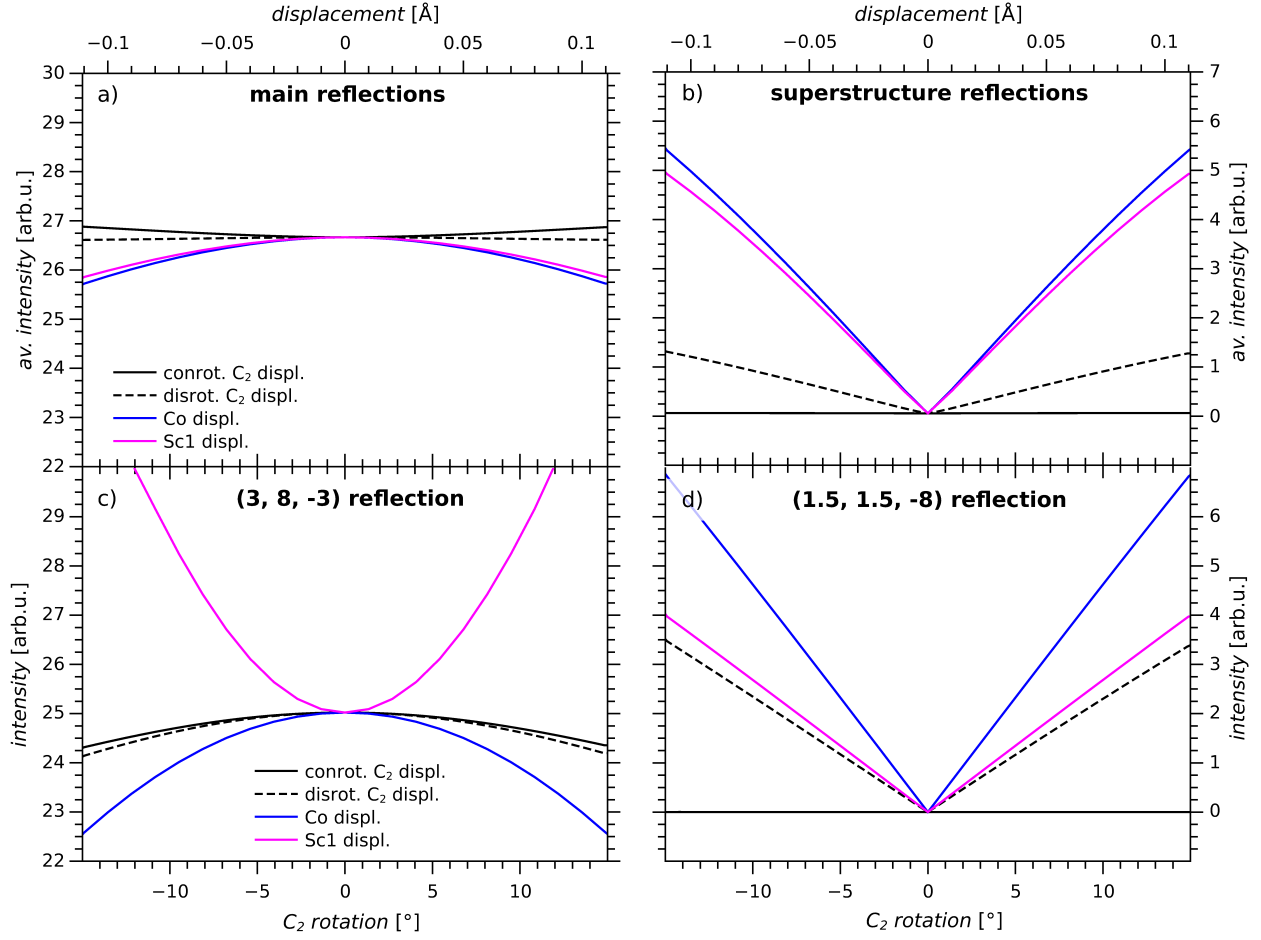


FIG. S23. Impact of conrotatory and disrotatory C_2 displacements (solid and dashed black lines), cobalt (blue line) and scandium atom displacements (magenta line) from their HT phase positions on the averaged intensity of (a) main and (b) superstructure reflections. The according effect on the intensity of an exemplary reflection from each of these categories is illustrated in (c) for the main reflection $(3, 8, -3)$ and (d) for the superstructure reflection $(1.5, 1.5, -8)$. Carbon atom displacements corresponding to each C_2 rotation (lower abscissa) are specified on the upper abscissa.

C. Reliability of the refined atom displacements

We examined the significance of the observed changes in the rotation angles of the C_2 units between 0 GPa and 4 GPa (experiment 3 in Tab. II) in more detail. The use of a closed-cycle sample cryostat and a diamond anvil cell (DAC) in our low-temperature x-ray diffraction experiments reduces the achievable data quality in various ways, *e.g.* by a limitation of the accessible reciprocal space and by parasitic scattering from the beryllium vacuum shroud (see Sec. VI for more details). To examine the effect of these factors, we collected low-temperature x-ray diffraction data sets ($T < 40$ K and $T \approx 100$ K) for a Sc_3CoC_4 single crystal inside a DAC before and after filling the cell with a pressure transmitting medium and application of 4 GPa. In agreement with our results for a single-crystalline Sc_3CoC_4 needle without surrounding pressure cell ($T = 11$ K and 100 K, experiment 1 in Tab. II) structural refinements on the ambient-pressure DAC data ($T = 36$ K and 106 K) point out conrotatory displacements of neighboring C_2 units along the $[Co(C_2)_2]_\infty$ ribbons with clearly non-zero rotation angles between $6(2)^\circ$ and $7(2)^\circ$ (all angles are specified with their threefold standard deviation). Overlays of the structural models of the ambient-pressure low-temperature phase obtained without and with surrounding DAC are given in Fig. S24a ($T < 40$ K) and Fig. S24b ($T \approx 100$ K). Crystal and refinement details, fractional coordinates and mean-square atomic displacement parameters are compared in Tab. XIII and Tab. XIV ($T < 40$ K), and Tab. XV and Tab. XVI ($T \approx 100$ K).

Furthermore, we checked the sensitivity of the fit quality indicator wR_{obs} (weighted R value) in structural refinements of the x-ray diffraction data collected with and without DAC to changes in the C_2 rotation angles (see Fig. S25 for $T < 40$ K and Fig. S26 for $T \approx 100$ K). To this end, the rotation angles of the two symmetry-independent C_2 units in the LT phase structure of Sc_3CoC_4 were constrained to follow conrotatory or disrotatory displacement patterns. After an initial relaxation the structural model was kept rigid and the value of wR_{obs} was recorded while incrementing the C_2 rotation angle in 0.1° steps between -15° and 15° .

The course of wR_{obs} with varying rotation angle at ambient pressure without DAC is indicated by dashed lines in Fig. S25a and Fig. S26a. Conrotatory displacements of neighboring C_2 units lead to a curve with two minima (black lines), whereas disrotatory displacements lead to a curve with a single minimum (orange lines). Consistent with the results

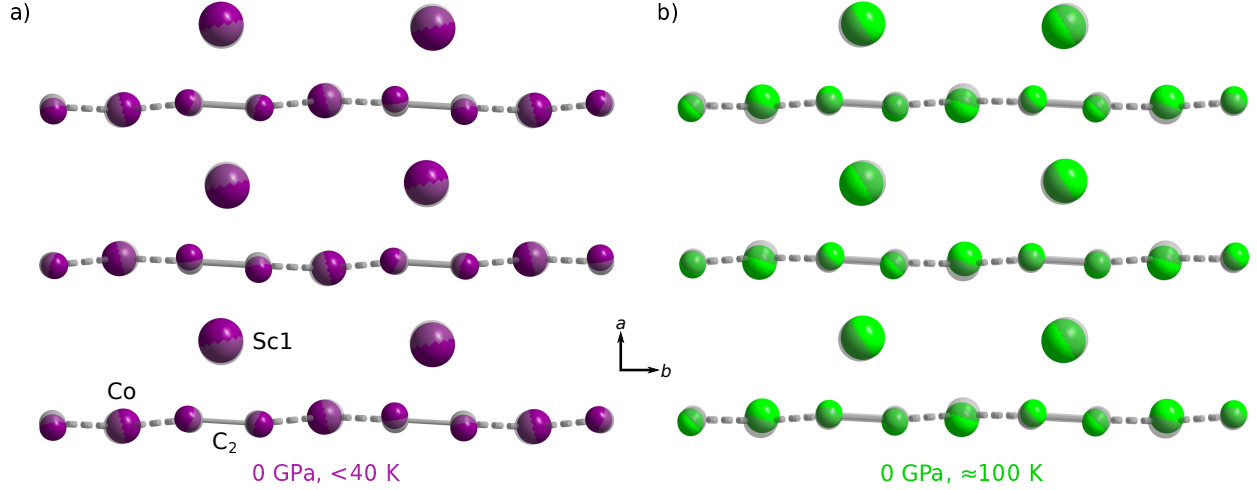


FIG. S24. Overlays of the refined atom positions within a layered building unit of Sc_3CoC_4 at low temperatures and 0 GPa without (gray, semi-transparent) and with surrounding pressure cell (colored, non-transparent). In (a) the atom positions at below 40 K (without DAC: 11 K, with DAC: 36 K) are compared, and in (b) the atom positions at approx. 100 K (without DAC: 100 K, with DAC: 106 K). Note that all atom displacements are exaggerated seven-fold and that Sc2 and Sc3 atoms have been omitted for clarity. The given coordinate system refers to the orthorhombic unit cell of the high-temperature phase.

of unconstrained refinements (marked by black open circles) the minima in wR_{obs} for disrotatory displacements at 0° are located at slightly higher wR_{obs} values than the minima at non-zero angles for conrotatory displacements ($T = 11\text{ K}$: $\Delta wR_{\text{obs}} = 0.35$; $T = 100\text{ K}$: $\Delta wR_{\text{obs}} = 0.13$). This wR_{obs} difference between the minima of the curves for conrotatory and disrotatory C_2 displacements degrades for the low-temperature DAC measurements at 0 GPa ($T = 36\text{ K}$: $\Delta wR_{\text{obs}} = -0.02$; $T = 106\text{ K}$: $\Delta wR_{\text{obs}} = 0.11$), although an unconstrained refinement still reliably converges to a structural model with conrotatory displacements and non-zero rotation angles (filled circles). Still, the flat course of wR_{obs} with varying conrotatory C_2 displacements directly relates to the large (threefold) standard deviation of the obtained rotation angles in the range of 2° . Applying a pressure of 4 GPa makes the situation much more clear-cut (see Fig. S25b for $T = 37\text{ K}$ and Fig. S26b for $T = 107\text{ K}$): Both, the curves for conrotatory (solid black lines) and disrotatory C_2 unit displacements (solid orange lines) have a substantial curvature and a single minimum close to 0° in confirmation of the results of unconstrained structural refinements (filled black circles).

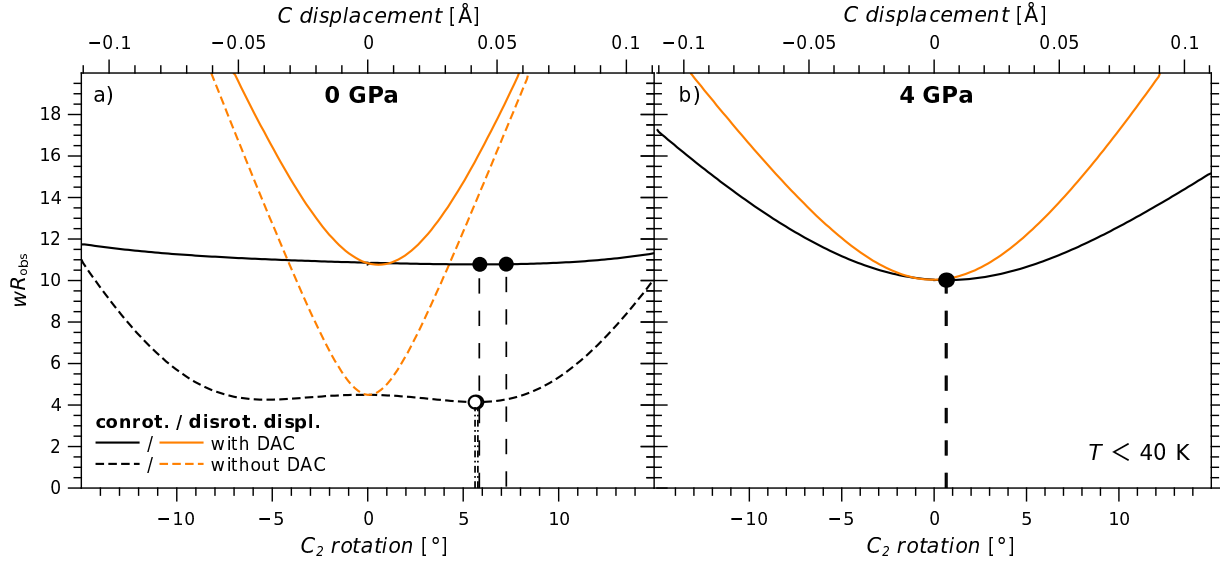


FIG. S25. Variation of the weighted R value wR_{obs} with the rotation angle of the C_2 units (lower abscissa) or the corresponding carbon atom displacement (upper abscissa) in rigid structural models for different low-temperature x-ray diffraction data sets (see text for more detailed explanation). In (a) the behavior of wR_{obs} for ambient-pressure data sets collected without ($T = 11$ K, dashed lines) and with ($T = 36$ K, solid lines) pressure cell is given, while (b) shows the behavior for a 4 GPa data set ($T = 37$ K, solid lines). In each case, the rotation angles of neighboring symmetry-independent C_2 units were constrained to follow conrotatory (black lines) or disrotatory displacement patterns (orange lines). Rotation angles obtained from unconstrained structural refinements are indicated by open and filled black circles.

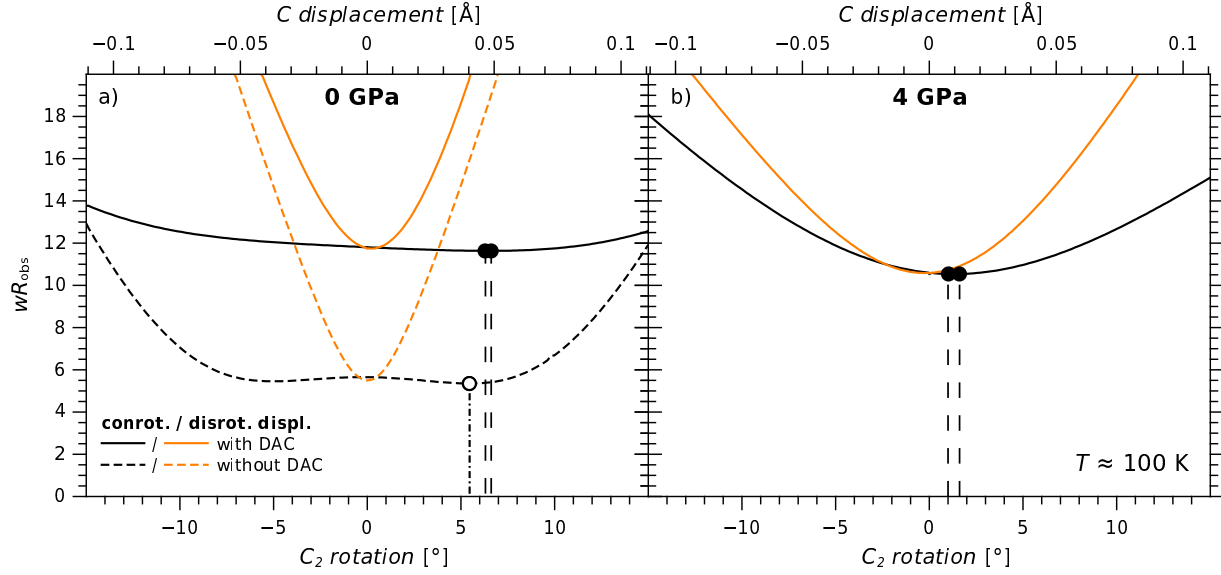


FIG. S26. Variation of the weighted R value wR_{obs} with the rotation angle of the C_2 units (lower abscissa) or the corresponding carbon atom displacement (upper abscissa) in rigid structural models for different low-temperature x-ray diffraction data sets. In (a) the behavior of wR_{obs} for ambient-pressure data sets collected without ($T = 100$ K, dashed lines) and with ($T = 106$ K, solid lines) pressure cell is given, while (b) shows the behavior for a 4 GPa data set ($T = 107$ K, solid lines). In each case, the rotation angles of neighboring symmetry-independent C_2 units were constrained to follow conrotatory (black lines) or disrotatory displacement patterns (orange lines). Rotation angles obtained from unconstrained structural refinements are indicated by open and filled black circles.

DAC	no	yes
	$a = 5.53630(10) \text{ \AA}$	$a = 5.53940(10) \text{ \AA}$
	$b = 12.0210(2) \text{ \AA}$	$b = 12.0309(2) \text{ \AA}$
unit cell dimensions	$c = 5.53640(10) \text{ \AA}$	$c = 5.53850(10) \text{ \AA}$
	$\beta = 104.8070(10)^\circ$	$\beta = 104.8280(10)^\circ$
	$V = 356.222(11) \text{ \AA}^3$	$V = 356.816(11) \text{ \AA}^3$
calculated density	$4.5095 \text{ g}\cdot\text{cm}^{-3}$	$4.502 \text{ g}\cdot\text{cm}^{-3}$
crystal size	$40 \times 51 \times 290 \text{ \mu m}^3$	$68 \times 116 \times 126 \text{ \mu m}^3$
wave length	0.56087 \AA	
transm. ratio (max/min)	$0.747 / 0.686$	$0.747 / 0.565$
absorption coefficient	5.016 mm^{-1}	5.007 mm^{-1}
$F(000)$	456	
θ range	3° to 36°	3° to 33°
range in hkl	-11/11, -25/25, -11/11	-6/10, -20/21, -6/10
total no. reflections	8720	1291
independent reflections	2142 ($R_{\text{int}} = 0.0123$)	390 ($R_{\text{int}} = 0.0101$)
reflections with $I \geq 2\sigma(I)$	2007	318
data / parameters	2142 / 43	318 / 19
goodness-of-fit on F^2	1.27	3.50
	$R = 0.0220$	$R = 0.0342$
final R indices [$I \geq 2\sigma(I)$]	$wR = 0.0414$	$wR = 0.1064$
	$R = 0.0271$	$R = 0.0342$
R indices (all data)	$wR = 0.0424$	$wR = 0.1064$
extinction coefficient	$0.0461(14)$	–
largest diff. peak and hole	$1.97 / -2.18 \text{ e}\cdot\text{\AA}^{-3}$	$0.41 / -0.43 \text{ e}\cdot\text{\AA}^{-3}$

TABLE XIII. Crystal data and structure refinements for ambient-pressure single-crystal x-ray diffraction experiments without ($T = 11 \text{ K}$) and with surrounding unpressurized Tozer-type diamond anvil cell ($T = 36 \text{ K}$).

atom	DAC	fractional atomic coordinates			$U_{\text{iso}}/U_{\text{eq}}$
		x	y	z	$[\text{\AA}^2]$
Co	no	0.26595(2)	0	0.26673(2)	0.00204(3)
	yes	0.26649(12)	0	0.26564(12)	0.0026(2)
Sc1	no	0.75582(3)	0	0.24273(3)	0.00207(6)
	yes	0.75700(14)	0	0.24355(13)	0.0029(3)
Sc2	no	0	0.187417(10)	0	0.00210(9)
	yes	0	0.18746(6)	0	0.0029(3)
Sc3	no	0	0.311540(10)	0.5	0.00210(9)
	yes	0	0.31145(6)	0.5	0.0030(3)
C1	no	0.4110(3)	0.12557(5)	0.0766(2)	0.0031(2)
	yes	0.410(3)	0.1257(2)	0.077(3)	0.0049(5)
C2	no	0.0889(3)	0.12487(5)	0.4233(2)	0.0030(2)
	yes	0.091(3)	0.1251(2)	0.425(3)	0.0049(5)

TABLE XIV. Refined fractional atomic coordinates and mean-square atomic displacement parameters obtained from low-temperature single-crystal x-ray diffraction experiments without ($T = 11$ K) and with surrounding unpressurized Tozer-type diamond anvil cell (DAC; $T = 36$ K). Note that the fractional coordinates refined from DAC data have been transformed in order to correspond to the same twin individual as the coordinates from non-DAC data.

DAC	no	yes
	$a = 5.53720(10) \text{ \AA}$	$a = 5.5386(2) \text{ \AA}$
	$b = 12.00370(10) \text{ \AA}$	$b = 12.0071(3) \text{ \AA}$
unit cell dimensions	$c = 5.53710(10) \text{ \AA}$	$c = 5.5365(2) \text{ \AA}$
	$\beta = 104.4620(10)^\circ$	$\beta = 104.386(2)^\circ$
	$V = 356.372(10) \text{ \AA}^3$	$V = 356.65(2) \text{ \AA}^3$
calculated density	$4.5076 \text{ g}\cdot\text{cm}^{-3}$	$4.5041 \text{ g}\cdot\text{cm}^{-3}$
crystal size	$40 \times 51 \times 290 \text{ \mu m}^3$	$68 \times 116 \times 126 \text{ \mu m}^3$
wave length	0.56087 \AA	
transm. ratio (max/min)	$0.747 / 0.646$	$0.746 / 0.583$
absorption coefficient	5.014 mm^{-1}	5.01 mm^{-1}
$F(000)$	456	
θ range	3° to 37°	3° to 32°
range in hkl	$-11/11, -25/25, -11/11$	$-6/10, -21/21, -6/10$
total no. reflections	8509	1234
independent reflections	2153 ($R_{\text{int}} = 0.0148$)	394 ($R_{\text{int}} = 0.0143$)
reflections with $I \geq 2\sigma(I)$	1947	291
data / parameters	2153 / 43	291 / 19
goodness-of-fit on F^2	1.44	3.25
final R indices [$I \geq 2\sigma(I)$]	$R = 0.0302$	$R = 0.0437$
	$wR = 0.0535$	$wR = 0.1153$
R indices (all data)	$R = 0.0389$	$R = 0.0437$
	$wR = 0.0549$	$wR = 0.1153$
extinction coefficient	$0.0231(15)$	–
largest diff. peak and hole	$1.94 / -2.20 \text{ e}\cdot\text{\AA}^{-3}$	$0.42 / -0.47 \text{ e}\cdot\text{\AA}^{-3}$

TABLE XV. Crystal data and structure refinements for ambient-pressure single-crystal x-ray diffraction experiments without ($T = 100 \text{ K}$) and with surrounding unpressurized Tozer-type diamond anvil cell ($T = 106 \text{ K}$).

atom	DAC	fractional atomic coordinates			$U_{\text{iso}}/U_{\text{eq}}$
		x	y	z	[\AA^2]
Co	no	0.25987(2)	0	0.26046(2)	0.00243(5)
	yes	0.25814(11)	0	0.25757(11)	0.0033(3)
Sc1	no	0.75383(3)	0	0.24498(3)	0.00239(10)
	yes	0.75366(14)	0	0.24668(13)	0.0034(3)
Sc2	no	0	0.187747(13)	0	0.00233(10)
	yes	0	0.18785(6)	0	0.0036(3)
Sc3	no	0	0.311642(13)	0.5	0.00235(10)
	yes	0	0.31168(6)	0.5	0.0035(3)
C1	no	0.4109(3)	0.12514(5)	0.0773(3)	0.0033(3)
	yes	0.4103(19)	0.1247(2)	0.076(2)	0.0047(6)
C2	no	0.0890(3)	0.12471(5)	0.4228(3)	0.0033(3)
	yes	0.0893(19)	0.1247(2)	0.425(2)	0.0047(6)

TABLE XVI. Refined fractional atomic coordinates and mean-square atomic displacement parameters obtained from low-temperature single-crystal x-ray diffraction experiments without ($T = 100$ K) and with surrounding unpressurized Tozer-type diamond anvil cell (DAC; $T = 106$ K). Note that the fractional coordinates refined from DAC data have been transformed in order to correspond to the same twin individual as the coordinates from non-DAC data.

D. Differences between twin domains

Single crystals of Sc_3CoC_4 are subjected to systematic twinning in the phase transition from the high-temperature (HT) to the low-temperature (LT) phase. This twinning process is due to a $t2$ step followed by an $i2$ step in the symmetry reduction (*translationengleiche* and isomorphic group-subgroup relationship, respectively) from the orthorhombic space-group $Immm$ of the HT phase structure to the monoclinic space-group $C2/m$ of the LT phase structure.^{2,35} An exemplary twinning operation that transforms the atomic positions in one twin domain into the atomic positions of the other is a m plane perpendicular to the a axis of the orthorhombic HT unit cell ($[[[-1\ 0\ 0], [0\ 1\ 0], [0\ 0\ 1]]]$). Its effect is demonstrated for the structural models of the LT phase at 0 GPa and 11 K (Fig. S27a) and at 4 GPa and 37 K (Fig. S27b). Whereas the twin domains at 0 GPa can be differentiated easily by the sense of rotation of the C_2 units, this is barely possible for the (hypothetical) twin domains with nearly unrotated C_2 units at 4 GPa.

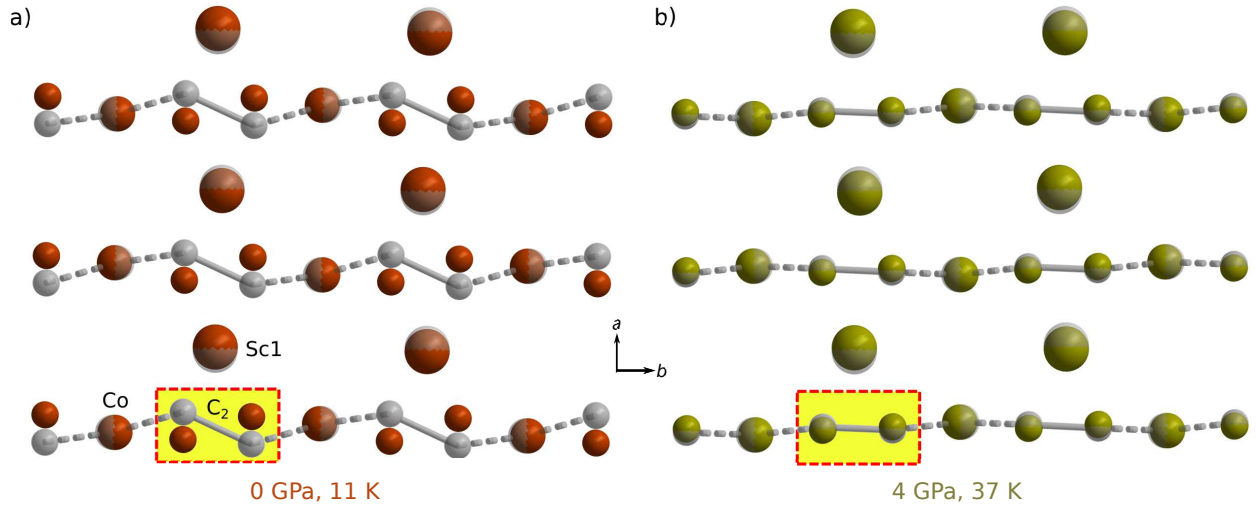


FIG. S27. Overlay of the atomic positions within the possible twin domains 1 (colored, non-transparent spheres) and 2 (gray, semi-transparent spheres) of Sc_3CoC_4 (a) in its ambient-pressure and (b) in its high-pressure low-temperature phase. All atom displacements are exaggerated seven-fold. For clarity, only the atoms within a layered building unit are shown, and Sc2 and Sc3 atoms have been omitted. The given coordinate system refers to the orthorhombic unit cell of the high-temperature phase.

-
- * georg.eickerling@uni-a.de
- † wolfgang.scherer@uni-a.de
- ¹ B. Rohrmoser, G. Eickerling, M. Presnitz, W. Scherer, V. Eyert, R.-D. Hoffmann, U. Rodewald, C. Vogt, and R. Pöttgen, *J. Am. Chem. Soc.* **129**, 9356 (2007).
- ² C. Vogt, R.-D. Hoffmann, U. Rodewald, G. Eickerling, M. Presnitz, V. Eyert, W. Scherer, and R. Pöttgen, *Inorg. Chem.* **48**, 6436 (2009).
- ³ M. He, C. Wong, D. Shi, P. Tse, E.-W. Scheidt, G. Eickerling, W. Scherer, P. Sheng, and R. Lortz, *J. Phys.: Condens. Matter* **27**, 075702 (2015).
- ⁴ C. Haas, *Strukturelle und physikalische Charakterisierungen niederdimensionaler Metallborocarbide und Metallcarbide*, Ph.D. thesis, University of Augsburg (2019).
- ⁵ A. Jesche and P. Canfield, *Philos. Mag.* **94**, 2372 (2014).
- ⁶ N. Tateiwa, Y. Haga, T. Matsuda, and Z. Fisk, *J. Phys.: Conf. Ser.* **500**, 142032 (2014).
- ⁷ N. Tateiwa, Y. Haga, T. Matsuda, Z. Fisk, S. Ikeda, and H. Kobayashi, *Rev. Sci. Instrum.* **84**, 046105 (2013).
- ⁸ N. Tateiwa, Y. Haga, T. Matsuda, and Z. Fisk, *Rev. Sci. Instrum.* **83**, 053906 (2012).
- ⁹ N. Tateiwa, Y. Haga, Z. Fisk, and Y. Ōnuki, *Rev. Sci. Instrum.* **82**, 053906 (2011).
- ¹⁰ T. Kobayashi, H. Hidaka, H. Kotegawa, K. Fujiwara, and M. Eremets, *Rev. Sci. Instrum.* **78**, 023909 (2007).
- ¹¹ A. Eiling and J. Schilling, *J. Phys. F: Met. Phys.* **11**, 623 (1981).
- ¹² B. Bireckoven and J. Wittig, *J. Phys. E: Sci. Instrum.* **21**, 841 (1988).
- ¹³ K. Yokogawa, K. Murata, H. Yoshino, and S. Aoyama, *Jpn. J. Appl. Phys.* **46**, 3636 (2007).
- ¹⁴ K. Murata, K. Yokogawa, H. Yoshino, S. Klotz, P. Munsch, A. Irizawa, M. Nishiyama, K. Iizuka, T. Nanba, T. Okada, Y. Shiraga, and S. Aoyama, *Rev. Sci. Instrum.* **79**, 085101 (2008).
- ¹⁵ M. Nicklas, “Pressure probes” in *Strongly Correlated Systems: Experimental Techniques*, edited by A. Avella and F. Mancini (Springer Berlin Heidelberg, Berlin, Heidelberg, 2015) Chap. 6, pp. 173–204.
- ¹⁶ D. Schmitz, *Experimentelle Hochdruckstudien an metallorganischen Modellsystemen mit aktivierten Kohlenstoff-Wasserstoff oder Silizium-Wasserstoff Bindungen*, Ph.D. thesis, University of Augsburg (2018).

- ¹⁷ P. Willmott, D. Meister, S. Leake, M. Lange, A. Bergamaschi, M. Böge, M. Calvi, C. Cancellieri, N. Casati, A. Cervellino, Q. Chen, C. David, U. Flechsig, F. Gozzo, B. Henrich, S. Jäggi-Spielmann, B. Jakob, I. Kalichava, P. Karvinen, J. Krempasky, A. Lüdeke, R. Lüscher, S. Maag, C. Quitmann, M. Reinle-Schmitt, T. Schmidt, B. Schmitt, A. Streun, I. Vartiainen, M. Vitins, X. Wang, and R. Wulschleger, *J. Synchrotron Rad.* **20**, 667 (2013).
- ¹⁸ M. Fisch, A. Lanza, P. Macchi, and N. Casati, *J. Appl. Cryst.* **48**, 1956 (2015).
- ¹⁹ A. Bergamaschi, A. Cervellino, R. Dinapoli, F. Gozzo, B. Henrich, I. Johnson, P. Kraft, A. Mozanica, B. Schmitt, and X. Shi, *J. Synchrotron Rad.* **17**, 653 (2010).
- ²⁰ G. Piermarini, S. Block, and J. Barnett, *J. Appl. Phys.* **44**, 5377 (1973).
- ²¹ R. Angel, D. Allan, R. Miletich, and L. Finger, *J. Appl. Cryst.* **30**, 461 (1997).
- ²² A. Le Bail, H. Duroy, and J. Fourquet, *Mater. Res. Bull.* **23**, 447 (1988).
- ²³ V. Petříček, M. Dušek, and L. Palatinus, *Z. Kristallogr.* **229**, 345 (2014).
- ²⁴ J.-F. Béjar and P. Lelann, *J. Appl. Cryst.* **24**, 1 (1991).
- ²⁵ D. Graf, R. Stillwell, K. Purcell, and S. Tozer, *High Pressure Res.* **31**, 533 (2011).
- ²⁶ R. Boehler, *Rev. Sci. Instrum.* **77**, 115103 (2006).
- ²⁷ R. Boehler and K. De Hantsetters, *High Pressure Res.* **24**, 391 (2004).
- ²⁸ G. Piermarini, S. Block, J. Barnett, and R. Forman, *J. Appl. Phys.* **46**, 2774 (1975).
- ²⁹ A. Dewaele, M. Torrent, P. Loubeyre, and M. Mezouar, *Phys. Rev. B* **78**, 104102 (2008).
- ³⁰ I. Kantor, “Fluorescence pressure calculation and thermocouple tools,” [online; accessed 14-December-2020].
- ³¹ A. Duisenberg, *J. Appl. Cryst.* **25**, 92 (1992).
- ³² A. Duisenberg, L. Kroon-Batenburg, and A. Schreurs, *J. Appl. Cryst.* **36**, 220 (2003).
- ³³ L. Krause, R. Herbst-Irmer, G. Sheldrick, and D. Stalke, *J. Appl. Cryst.* **48**, 3 (2015).
- ³⁴ K. Murata and S. Aoki, *Rev. High Pressure Sci. Technol.* **26**, 3 (2016).
- ³⁵ G. Eickerling, C. Hauf, E.-W. Scheidt, L. Reichardt, C. Schneider, A. Muñoz, S. Lopez-Moreno, A. H. Romero, F. Porcher, G. André, R. Pöttgen, and W. Scherer, *Z. Anorg. Allg. Chem.* **639**, 1985 (2013).